# Teleseismic P-waves at the AlpArray seismic network: Wave fronts, absolute traveltimes and traveltime residuals

Marcel Heinz Paffrath[1], Wolfgang Friederich[1], and the AlpArray and AlpArray-SWATH D Working Groups [*]

[1]Ruhr-Universität Bochum
[*]Full list of participants at the end of the paper.

**Correspondence:** Marcel Heinz Paffrath (marcel.paffrath@rub.de)

**Abstract.** We present an extensive dataset of highly accurate absolute traveltimes and traveltime residuals of teleseismic P-waves recorded by the AlpArray Seismic Network and complementary field experiments in the years from 2015 to 2019. The dataset is intended to serve as the basis for teleseismic traveltime tomography of the upper mantle below the greater Alpine region. In addition, the data may be used as constraints in full-waveform inversion of AlpArray recordings. The dataset comprises about 170.000 onsets derived from records filtered to an upper corner frequency of $0.5\,\text{Hz}$ and 214.000 onsets from records filtered to an upper corner frequency of $0.1\,\text{Hz}$. The high accuracy of absolute and residual traveltimes was obtained by applying a specially designed combination of automatic picking, waveform cross-correlation and beamforming. Taking traveltime data for individual events, we are able to visualize in detail the wave fronts of teleseismic P-waves as they propagate across AlpArray. Variations of distances between isochrons indicate structural perturbations in the mantle below. Traveltime residuals for individual events exhibit spatially coherent patterns that prove to be stable if events of similar epicentral distance and azimuth are considered. When residuals for all available events are stacked, conspicuous areas of negative residuals emerge that already indicate the lateral location of subducting slabs beneath the Apennines and the western, central and eastern Alps. Stacking residuals for events from 90 degree wide azimuthal sectors results in lateral distributions of negative and positive residuals that are generally consistent but differ in detail due to the differing direction of illumination of mantle structures by the incident P-waves. Uncertainties of traveltime residuals are estimated from the peak width of the cross-correlation function and its maximum value. The median uncertainty is $0.15\,\text{s}$ at $0.5\,\text{Hz}$ and $0.18\,\text{s}$ at $0.1\,\text{Hz}$, which is more than 10 times lower than the typical traveltime residuals of up to $\pm 2\,\text{s}$. Uncertainties display a regional dependence caused by quality differences between temporary and permanent stations as well as site-specific noise conditions.

## 1 Introduction

The recently acquired AlpArray data set provides a fascinating opportunity to extend our knowledge on the structure of the upper mantle below the greater Alpine area, and in particular to answer long-standing questions regarding the orientation and penetration of lithospheric slabs, their connection to the well-studied crustal structure and their influence on surface processes. AlpArray (Hetényi et al., 2018) is a multinational consortium built from 36 institutions from 11 countries dedicated to research
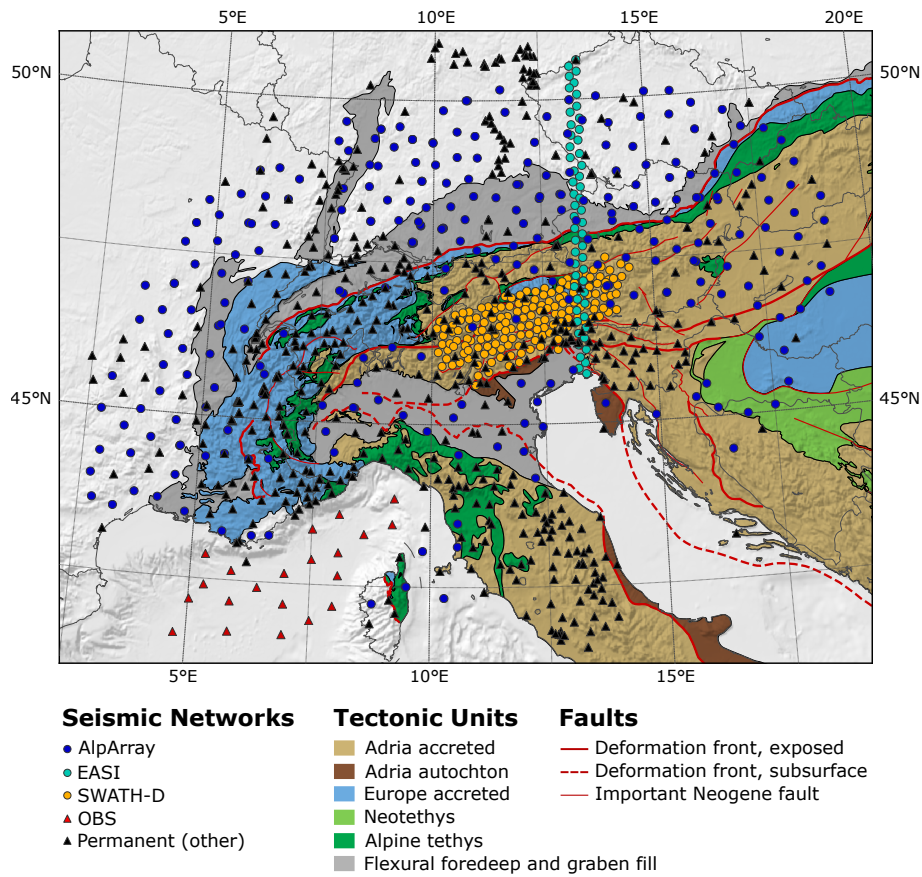
**Figure 1.** Tectonic map of the Alpine chains compiled by M.R. Handy showing different seismic networks and temporary experiments, tectonic units and major fault systems.

on the greater Alpine orogenic system encompassing the Alps, the Apennines, the Carpathians and the Dinarides (Fig. 1). The backbone is the AlpArray Seismic Network, consisting of up to 600 seismic broadband stations operated in changing configurations since 2015. With the Alps at its centre, the array reaches from the Po plain to the river Main in Germany, and from the Massif Central to the Pannonian basin. The array is constructed on a foundation of permanent stations with temporary stations deployed to fill gaps and thus produce a rather regular array with about 50 km station spacing. In addition, complementary targeted array experiments were carried out: ocean bottom seismometers were deployed in the Ligurian Sea and even denser subarrays were installed in the southern Central and Eastern Alps (Heit et al., 2017) and along the $13.4°$E meridian (EASI, 2014).

To tackle the challenging research opportunities offered by the AlpArray data with regard to Alpine mantle structure, travel-time tomography of teleseismic body waves certainly belongs to the methods of choice (e.g., Mitterbauer et al., 2011; Lippitsch et al., 2003). In teleseismic tomography, the variation of arrival times of body waves from distant earthquakes across the array are inverted for velocity perturbations below the array. Models obtained with this technique using regional arrays are typically

confined to the upper mantle. For the AlpArray Seismic network the lower bound is around $600\,\text{km}$ depth. Imagining a spherical chunk with a lateral extension similar to that of the seismic array (up to $\sim 10°$), below this depth only about one fourth of the horizontal area spanned by this chunk is penetrated by intersecting rays and smearing of anomalies along the rays will be the consequence for the remaining area. Controlled by the lateral extension of the array, ray-crossing becomes insufficient below

40     this depth and anomalies will start to smear in depth perpendicular to the wave front, i.e. structures will not be illuminated from opposite directions anymore. Lateral resolution is limited by the station spacing of the array. The method is mainly sensitive to volumetric perturbations of seismic velocity and does not give constraints on the location of internal discontinuities. It has been used in many studies on mantle structure, for example Koulakov et al. (2002); Lippitsch et al. (2003); Piromallo and Morelli (2003).

45     A method which reaches beyond teleseismic tomography is full waveform inversion (FWI) where entire or partial waveforms are inverted for velocity and also density perturbations (e.g., Mora, 1987; Tromp et al., 2005; Fichtner et al., 2009; Zhu et al., 2012; Butzer et al., 2013; Zhu et al., 2015; Schumacher et al., 2016). Predictions of waveforms for given velocity models are obtained by full 3D numerical forward modelling making the method very expensive with regard to storage requirements and computation time. When applied to teleseismic body waves, hybrid approaches are invoked to make the method numerically

50     tractable (e.g., Monteiller et al., 2013; Tong et al., 2014a, b): full 3D forward modelling is only done in a regional box below the array while wave propagation from the distant earthquake to this box is done by less expensive methods which however assume laterally homogeneous or axially symmetric earth structure.

    One basic preparatory step for both methods is the determination of traveltimes. While the need of traveltimes is obvious for traveltime tomography, also teleseismic full waveform inversion can benefit from traveltimes in two different ways. First of all,

55     FWI requires a good (ideally 3-D) starting model to ensure that the inversion converges to the global minimum. This model can be obtained from a traveltime tomography. Secondly, since the waveforms are typically band-passed to some (narrow) frequency range, they become monochromatic and waveform matching may suffer from cycle skipping. In such a situation, absolute traveltimes as additional constraints can help to make waveform matching less ambiguous. Traditionally, arrival times were determined by manual reading of onset times from seismic records, but it is well-known that even manual readings

60     are affected by different reading styles of analysts (e.g., Douglas et al., 1997; Diehl et al., 2009b) and, hence, may suffer from substantial inconsistencies. Moreover, manual reading of hundreds of thousands of records would require a forbidding amount of human effort. To cope with the ever increasing number of available seismic stations, automatic procedures have been developed to determine arrival times.

    One of the first automatic picking procedures that is still used as a fast signal detection method was introduced by Allen

65     (1978, 1982). It is based on a characteristic function (CF) which is calculated as the ratio of the average of a signal within a short time window to that in a long time window (STA/LTA). The CF rises as soon as a signal with a higher amplitude than the preceding noise is encountered in the short time average window. Baer and Kradolfer (1987) developed an automatic phase picker by modifying Allen's characteristic function and implementing a dynamic threshold. The algorithm developed by Küperkoch et al. (2010) modifies and applies the scheme of Saragiotis et al. (2002). Kurtosis or skewness of a seismogram

70     is calculated in a moving window and the Akaike Information Criterion (Akaike, 1971, 1974) is applied to the resulting CF.

These approaches work well in the context of local to regional scales and have been used for earthquake location and local earthquake tomography methods. In the case of teleseismic tomography, one can benefit from nearly planar wave fronts and similar waveforms to improve traveltime measurements by cross-correlation of waveforms (e.g., Rowe et al., 2002; Mitterbauer et al., 2011). Especially in view of the newly available dense seismic arrays and our quest for ever improving spatial resolution of tomographic models, the accuracy of traveltime measurements plays an increasingly important role. Correlation techniques have been developed where selected wave packets of two different records of similar waveforms are correlated to determine their relative time shift. VanDecar and Crosson (1990) developed a multi-channel cross-correlation technique (MCCC), to receive high precision relative arrival times, by correlating each trace with every other. This method was also used in a recent study by Zhao et al. (2016), where a finite-frequency kernel method was used for a tomography of the central European subsurface. However, this method does not produce absolute arrival times, which are a prerequisite for the stabilisation of the FWI.

In this paper, we confirm that even advanced techniques of automatic reading of arrival times do not reach the accuracy required by teleseismic traveltime tomography on dense arrays. Using AlpArray data, we demonstrate that an appropriate combination of automatic picking, correlation measurements and beamforming can attain the required accuracy and provide both reliable traveltime residuals and absolute traveltimes. Applying this technique, we are able to map the propagation of P-wave fronts across the AlpArray network and to obtain sufficiently accurate traveltime residuals at all stations of the network. By analysing records of hundreds of teleseismic earthquakes, we can show the coherency and reproducibility of the residuals and study their dependency on event azimuth and frequency. Stacking of event-specific traveltime residuals yields very stable patterns that already show, prior to any tomography inversion, where high- and low velocity anomalies have to be expected in the upper mantle. We shall use these time measurements in a later study for performing a teleseismic tomography and full waveform inversion.

## 2   Data Basis

Deployment of the main AlpArray backbone network Z3 was started in 2015 (Fig. 1) with the aim to close gaps in the existing permanent networks for a recording period of at least three years by installing over 280 temporary broadband seismometers. Among these are 24 ocean bottom seismometers deployed by the LOBSTER and the AlpArray-FR project for a period of 8 months from June 2017 to February 2018 closing a large station gap in the Ligurian Sea. The earliest complementary experiment, partly included in our dataset, is the Eastern Alpine Seismic Investigation (EASI) project with 55 stations deployed on a north south profile at $13.4°$E crossing the Alps from the northern Alpine foreland to the Adriatic Sea which recorded ground motion for more than a year until August 2015. The second complementary experiment SWATH-D was carried out for two years starting at the end of 2017, further increasing station density in a key area of the central and eastern Alps, directly above a Moho offset (Gebrande et al., 2001; Spada et al., 2013), a possible slab gap and slab polarity switch (Lippitsch et al., 2003), thereby adding another 154 seismic broadband stations to our dataset. Finally, we extended the coverage of our database to the north and south by adding permanent stations in central Germany and northern Italy, thus obtaining a total of

1025 different seismic broadband stations with recording times scattered through a period of over four and a half years between
2015 and the end of 2019, with a peak in station coverage of more than 720 stations in late 2017.

## 2.1 Teleseismic Tomography Database

From the available data described above, we assembled records suitable for teleseismic tomography of 974 teleseismic earth-
quakes with origin times between January 2015 and July 2019 and moment magnitude 5.5 or higher. They encompass wave-
forms of all stations available in a $5°$ radius around a central position in the Alps located at $46°N$ and $11°E$. Out of these we
evaluated mantle phases for 765 events, all within distances between $35°$ and $135°$ relative to the central position, leading to a
minimum event distance of $30°$ for the closest and a maximum event distance of $140°$ for the farthest station. Information on
location and moment tensor was taken from the Global CMT catalogue distributed by the Lamont-Doherty Earth Observatory
(LDEO) of Columbia University (Dziewonski et al., 1981; Ekström et al., 2012).

We produced a high frequency dataset ($db_{0.5}$) using a 4th-order Butterworth bandpass filter between $0.03\,Hz$ and $0.5\,Hz$,
which turned out to be perfectly suited for combining automatic picking and cross-correlation of land stations records. Since,
however, oceanic microseismic noise is rather strong in this frequency band, cross-correlation of OBS records was only possible
for very strong earthquakes. For this reason, we assembled a second, low frequency dataset ($db_{0.1}$) with bandpass filter upper
corner frequency of $0.1\,Hz$. In this way, most of the oceanic microseismic noise could be avoided, however at the expense of
pick accuracy and resolution of teleseismic tomography.

The distribution of earthquakes of both datasets relative to the Alps strongly varies with azimuth and epicentral distance.
Fig. 2 shows the distribution of 370 evens that were ultimately picked for the high-frequency dataset. Events that could not be
evaluated had a too low amplitude at the stations. Reasons for this were mainly the ratio between magnitude and distance as
well as the focal mechanisms. The majority of the recorded waves reach the Alps from a sector between north and east ($0°$
to $90°$) mainly originating from the Pacific Ring of Fire at epicentral distances between $80°$ and $90°$. A second concentration
of sources in a sector between WSW and WNW with azimuths between $230°$ and $290°$ is produced by earthquakes in the
subduction zones of North and South America. Epicentral distances in this sector are more broadly distributed than in the
NE sector. There is a remarkable lack of events in a sector between about $100°$ and $230°$ as well as in the opposite direction
between $290°$ and $340°$. To obtain at least a few usable records from the poorly covered sectors long recording periods are
essential.

## 3 Automatic determination of absolute traveltimes, traveltime residuals and uncertainties

In the following part, we will examine the capability of characteristic function picking algorithms to resolve traveltime residuals
with an accuracy required for traveltime tomography. We will show the most prominent difficulties and demonstrate how we
can benefit from a combination of the AIC algorithm, beamforming and cross-correlation. The resulting multi-stage algorithm
combines theoretical onset calculation for spherically symmetric earth models, characteristic function picking algorithms and
various steps of signal cross-correlation/beamforming to receive absolute as well as relative onsets with an uncertainty of
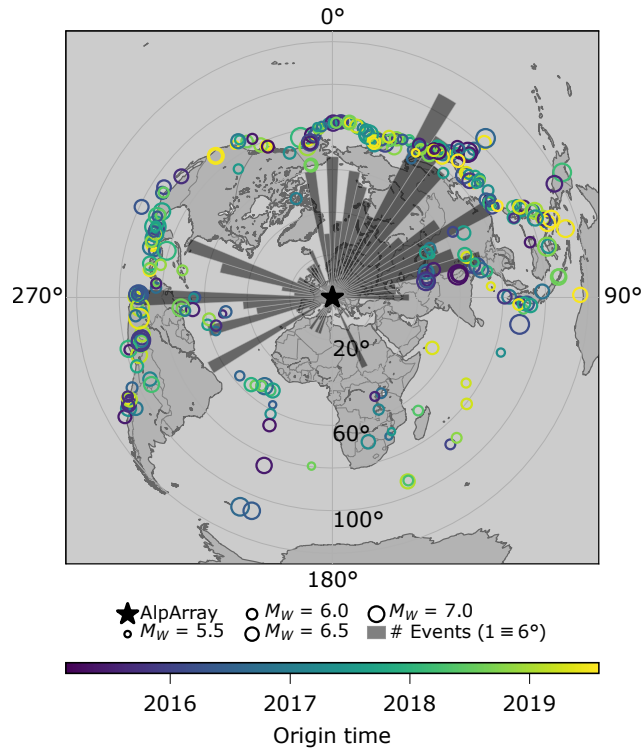
**Figure 2.** Event distribution of the high frequency dataset $db_{0.5}$. Size of circles correlates with moment magnitude, color with origin time. Histogram shows number of events binned in $5°$ bins azimuthally. A bar height of $60°$ radial distance equals 10 events coming from that direction. The distribution is very irregular with most events located in the northeastern quadrant and in a western sector. There are large gaps with few or no events especially from the southeast as well as from the northwest. Peak value is 18 events for the back-azimuth interval between $30°$ and $35°$.

fractions of a second. We also present an empiric way of automatic evaluation of uncertainties which has proven to be extremely robust.

## 3.1 Definitions and methodological approach

In the following, we will use the quantities absolute traveltime at some station, $\tau_j$, defined as the absolute arrival time minus source time, theoretical traveltime, $T_j$, defined as the time relative to the earthquake source time predicted by a standard earth model using an available earthquake location, and averages of these quantities over the entire array, $\overline{\tau}$ and $\overline{T}$, respectively. The traveltime residual is defined by

$$r_j = \tau_j - T_j - (\overline{\tau} - \overline{T}) = \tau_j - \overline{\tau} - (T_j - \overline{T}). \tag{1}$$

We subtract array averages of observed and theoretical traveltimes to form residuals, because pure differences between observed and theoretical traveltimes contain errors of source time and depend on the wave path through the entire earth. The difference

**6**

between the array averages, $\overline{\tau} - \overline{T}$, should take into account most of the heterogeneous earth structure remote from the array, while the remaining residuals after average subtraction should rather reflect influences of heterogeneities below the array.

The crucial question is, how to obtain highly accurate traveltime residuals and absolute traveltimes. If we were able to construct a low-noise beam trace (e.g., Van Veen and Buckley, 1988) associated with some selected reference station by stacking appropriately shifted waveforms of all or selected stations on top of the reference station trace, we could perform cross-correlation with all other traces and read a highly accurate absolute traveltime from the beam trace. Let us denote this time by $\tau_B$. The theoretical traveltime for the beam is of course equal to that of the reference station, i.e. $T_B = T_R$. Taking the difference of the traveltime residuals of some station trace, $r_j$, and the beam trace, $r_B$, we find using Eq. (1):

$$r_j - r_B = \tau_j - \tau_B - (T_j - T_B)$$
$$= \Delta\tau_{jB} - \Delta T_{jB} \quad \text{with} \quad \tau_j = \tau_B + \Delta\tau_{jB}, \tag{2}$$

and hence

$$r_j = r_B + \Delta\tau_{jB} - \Delta T_{jB} \quad \text{with} \quad r_B = \tau_B - \overline{\tau} - (T_B - \overline{T}), \tag{3}$$

where $\Delta\tau_{jB}$ is the difference between the absolute traveltime at station $j$ and the absolute beam time and $\Delta T_{jB}$ is the difference between the corresponding theoretical arrival times. We estimate $\Delta\tau_{jB}$ with high accuracy by cross-correlation of station and beam trace and obtain $\tau_B$ by automatic picking. From these two, we can calculate a highly accurate absolute traveltime for any station, $\tau_j = \tau_B + \Delta\tau_{jB}$, and the array average $\overline{\tau} = \tau_B + \overline{\Delta\tau_{jB}}$, finally allowing us to determine the beam residual, $r_B$, and the station residual $r_j$. Note that the error of the beam traveltime does not propagate into the beam residual, as it is also contained in the traveltime array average, $\overline{\tau}$, and subtracted when calculating $r_B$ according to Eq. (3). Thus, the accuracy of the residual is controlled by the accuracy of the $\Delta\tau_{jB}$ only.

To obtain the beam itself, we first select a reference station and consider traveltime differences to all other stations, $\tau_j - \tau_R$, which are again determined by cross-correlation. The reference station should be close to the center of the array to minimize waveform discrepancies to other stations, and exhibit a high data availability and low noise. We then use these time differences to shift the station traces and stack them on top of the reference trace to form the beam. Stacking is restricted to traces with sufficiently high correlation with the reference trace. To perform these initial cross-correlations efficiently, we take advantage of automatic readings at the stations based on higher-order statistics and the Akaike information criterion (Küperkoch et al., 2010).

In summary, we start with automatic picks at the stations, use them to efficiently determine the time differences to a reference trace by cross-correlation, then shift the traces accordingly to form the beam. The beam is automatically picked and cross-correlation with all traces is repeated to obtain absolute traveltimes and traveltime residuals according to eqs. (2) and (3), respectively.

## 3.2 Higher Order Statistics picking algorithm

To get initial P-wave onsets as reference times for cross-correlation in records of teleseismic earthquakes we use the HOS/AIC algorithm by Küperkoch et al. (2010), which is originally designed for precise local to regional earthquake detection, location and focal mechanism estimation but not for teleseismic phase reading. Therefore, all wavelength dependent parameters were adapted to our needs.

We choose kurtosis, the central moment of order $k = 4$, as characteristic function, which is calculated on a demeaned seismogram in a moving window of $N$ time samples at index $j$ as

$$\hat{m}_k(j) = \frac{1}{N} \sum_{l=0}^{N-1} x_{j-l}^k.$$  (4)

The AIC, which estimates the information loss of a function, is applied to the kurtosis function in the following way (Küperkoch et al., 2010):

$$
\begin{aligned}
AIC(k) = {} & (k-1) \lg \left( \frac{1}{k} \sum_{j=1}^{k} CF_j^2 \right) \\
& + (L-k+1) \lg \left( \frac{1}{L-k+1} \sum_{j=k}^{L} CF_j^2 \right),
\end{aligned}
$$  (5)

with $L$ being the length of the kurtosis function and $k$ ranging from $0$ to $L$. The minimum of the AIC in the calculation window is defined as the most probable pick (mpp) of the phase.

As initial guess, we use theoretical onsets of the phase estimated for a spherically symmetric earth model and calculate characteristic functions in a properly chosen time window around those onsets. We select the moving time window a full order of magnitude larger than those typically used for local earthquake onset determination, rendering it rather a growing than a moving window and calculate the most probable onset. Subsequently, an automatic quality is assigned to the onset based on the signal-to-noise ratio and the difference between the latest and earliest possible pick (Diehl et al., 2009b). This quality determines whether the pick is used for further processing. The earliest possible pick, $t_{epp}$, is calculated as half the signal period before the most probable pick, $t_{mpp}$, accounting for a possibly missed first oscillation before the most probable pick. The signal period for this step is estimated by the mean time differences of zero-crossings within a characteristic time window after the most probable pick. The latest possible pick, $t_{lpp}$, is set to the time where the signal amplitude exceeds the noise level which is calculated as the root mean square of the noise in a window preceding the most probable pick. A symmetrized pick error (SPE) is then calculated as a weighted average of both pick uncertainties with double weight on the uncertainty derived from the latest possible pick:

$$
\begin{aligned}
SPE &= \frac{\Delta t_{earliest} + 2\Delta t_{latest}}{3} \\
&= \frac{(t_{mpp} - t_{epp}) + 2(t_{lpp} - t_{mpp})}{3} \\
&= \frac{2t_{lpp} - t_{epp} - t_{mpp}}{3} .
\end{aligned}
$$  (6)

By definition, using a maximum frequency of $0.5\,\mathrm{Hz}$, we obtain a minimum uncertainty from the earliest possible pick of a full second. Assuming $\Delta t_{latest} = 0$, the minimum possible SPE will be $0.33\,\mathrm{s}$. However, more realistic uncertainties will likely range in the order of 1 to 2 seconds, which is already close to the maximum traveltime residuals expected from mantle heterogeneities below the Alpine orogen. In many cases, pick uncertainties even exceed typical traveltime residuals of interest (Fig. 5a). In order to take full advantage of the high station density of AlpArray, it is therefore crucial to reduce the uncertainties of our onsets.

We manually validated by visual inspections that the large uncertainties result from difficulties of the characteristic function algorithm to find that part of the first P-wave onset which is similar in all traces. The reason for this is the relatively low amplitude of the P-onset which is often overlain by different levels of station noise. The resulting most probable onsets therefore strongly scatter confirming estimated uncertainties of about one half of the signal period. Another downside of the characteristic function approach is the false picking of either later arriving phases due to the first motion being completely masked by noise, or of other signals produced in the vicinity of the station leading to a severe number of outliers and to a time-intensive manual postprocessing.

Despite being unusable for a direct estimation of teleseismic traveltime residuals, with their uncertainties of a few seconds, AIC onsets are still far superior to theoretical 1D earth model onsets as reference time for signal cross-correlation. We found that theoretical phase onsets can differ from actual arrivals by up to some tens of seconds, most probably owing to differences of the true physical parameters in the global earth to those of the spherically symmetric earth model, uncertainties in origin time, dispersion processes along the travel path, as well as to the use of centroid-times of the gCMT catalog as earthquake origin times (which we want to use for the FWI). The resulting need of large cross-correlation shifts to catch all overlapping phases would involve a high risk of cycle skipping.

An analysis of the necessary shift in traveltimes predicted by the standard earth model AK135 (Kennett et al., 1995) for the final picks of 370 events in a frequency band between $0.03\,\mathrm{Hz}$ and $0.5\,\mathrm{Hz}$ yielded an average value of $-3.71\,\mathrm{s}$, implying that the average traveltime in the area of study is less than predicted by the AK135 earth model. The standard deviation is $\sigma = 5.84\,\mathrm{s}$. We found an absolute time-shift of over $10\,\mathrm{s}$ for 22 events with a peak value of $-53\,\mathrm{s}$. Hence, it is not reasonable to directly use 1D theoretical onsets as starting points for a signal cross-correlation.

Especially for lower-magnitude events and high-noise OBS records it may happen for some stations that useful automatic picks are not available. Provided that there are sufficient records left with a reliable automatic pick, we go back to theoretical traveltimes as correlation reference times which have been corrected by the median time difference between the available automatic picks and the corresponding theoretical traveltimes. In this way, we still obtain good time references for cross-correlation and avoid omitting all records with unreliable automatic picks. This approach can greatly increase the yield of the cross-correlation technique.

## 3.3  Correlation Approach

Applying a cross-correlation method to improve first arrivals on a large regional array like the AlpArray seismic network is based on the hypothesis of a high similarity of the waveforms of the selected phase across the array. We found this requirement
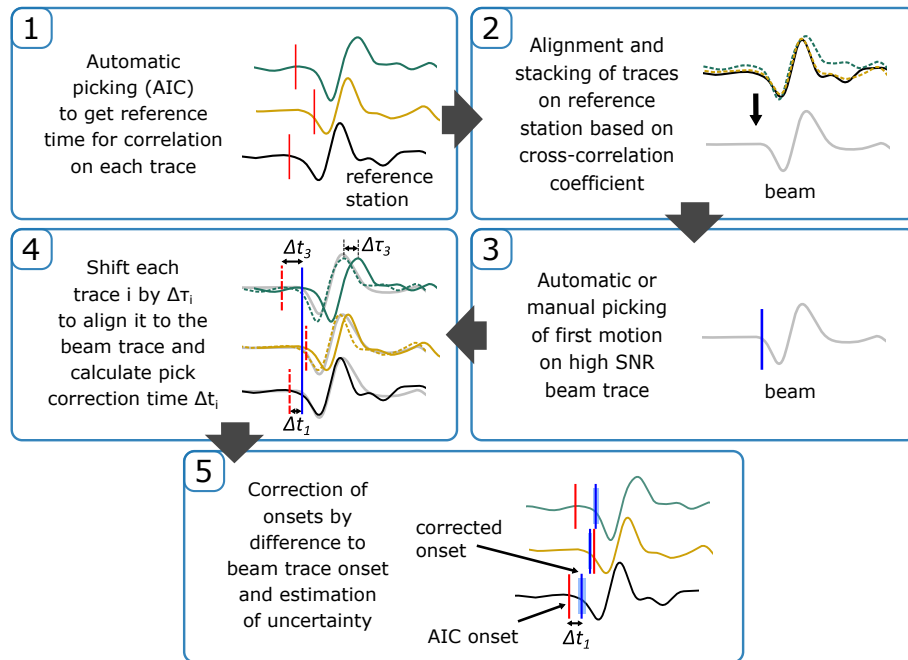
**Figure 3.** Workflow of the correlation picking algorithm. Solid lines show exemplary waveforms on three different stations. Black solid line shows reference station trace. Dashed lines of waveforms indicate that a waveform has been cut and shifted onto the reference (or beam) trace. Red vertical lines show reference AIC onset times, blue solid lines show corrected onsets.

to be satisfied especially well for teleseismic P-waves travelling through the mantle but not for PKP phases that penetrate the core. In contrast to mantle P-phases, PKP phases are composed of several arrivals which modify the shape of the waveform

240 across the array owing to the different epicentral distances making signal correlation challenging.

We start by searching for a reference station which represents the waveforms of the entire array best for each single event. The most important criterion for such a station is a continuous operation with a high data quality. Therefore, we only consider permanent stations with low noise that were ideally running for the entire time span of events in our database. Also we want this station to be in a central position in the Alps, with a low distance to all other stations it shall represent, to minimize

245 possible changes in waveform related to large scale heterogeneities in the global earth (see Sect. 3.1). For each event we start with a small pool of stations meeting those criteria and correlate the signals of all other stations in small time windows around the reference times we get from the AIC picks and the corrected theoretical traveltimes. The reference station with the highest mean correlation is then chosen to be representative of the full set of stations for this event. Combining each station selected for an event with all other available stations leads to 187.000 correlation pairs for the 370 events in our database. The

250 average cross-correlation coefficient for those signal pairs is $0.78$. After correlating all stations with the reference station, we align the waveforms according to the time of the maximum of the cross-correlation function. For each event we then form a beam representing the onset of the first P-wave phase by stacking the vertical component traces onto the reference station if
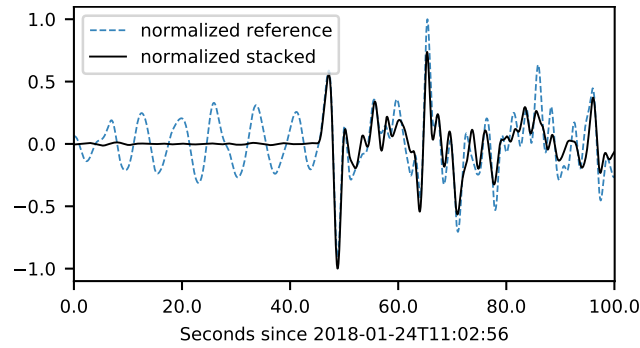
**Figure 4.** Stacking example for M6.1 earthquake in Hokkaido, Japan on 24 January 2018. 450 out of a total of 746 stations with a cross-correlation coefficient $> 0.8$ to the reference trace CH.PANIX (blue line) are stacked onto each other (black line). The first motion that was poorly resolvable on the reference trace can be clearly identified on the stacked trace, as the signal-to-noise ratio increased by a factor of 30 in the stacking process. Both traces are normalized for comparison and filtered between $0.03\,\mathrm{Hz}$ and $0.5\,\mathrm{Hz}$.

the maximum cross-correlation coefficient is above a certain threshold (Fig. 3). For this study, we chose a threshold of $0.8$. To find the exact time of highest correlation independent from sampling, a parabola is fitted around the concave part of the cross-correlation function and analytically evaluated for its apex (Deichmann and Garcia-Fernandez, 1992).

The resulting beam (Fig. 4) is of very high quality with an increase in signal-to-noise ratio (SNR) by a factor of about 30. On the beam, first motion becomes clearly visible and can be determined precisely using the automatic picking algorithm, which was done in this study. Alternatively, the reference onset can be determined by hand once for each event. After determination of the absolute pick on the beam, vertical components of all stations are correlated with it. The traveltime at each station is then calculated as the beam traveltime plus the time difference obtained from the lag time associated with the maximum correlation between the beam waveform and the waveform at the station. After onset determination our algorithm also searches for outliers within a time window around an expectation value we calculate for each station to further assess possible cycle-skipping issues. Finally, to assure the consistency of our traveltime dataset, wave fronts are constructed and visually inspected using plots similar to those shown in Fig. 8, where outliers can be easily recognized as they create strong distortions of the isochrones.

The different role of theoretical, AIC and correlation corrected traveltime is illustrated in Fig. 5. If the traces are aligned according to theoretical traveltime (Fig. 5a), the alignment with the beam trace is worst. Evidently, this must be due to lateral heterogeneities below the array not contained in the standard earth model. If the traces are aligned according to their AIC automatic pick (Fig. 5b), overlap with the beam trace improves but there are still significant deviations for example for stations Z3.A013A and Z3.A286A. The agreement with the stacked trace is best when the traces are aligned according to their correlation corrected onsets (Fig. 5c). This latter subfigure demonstrates the scatter of the AIC picks which makes them unsuitable for teleseismic tomography.
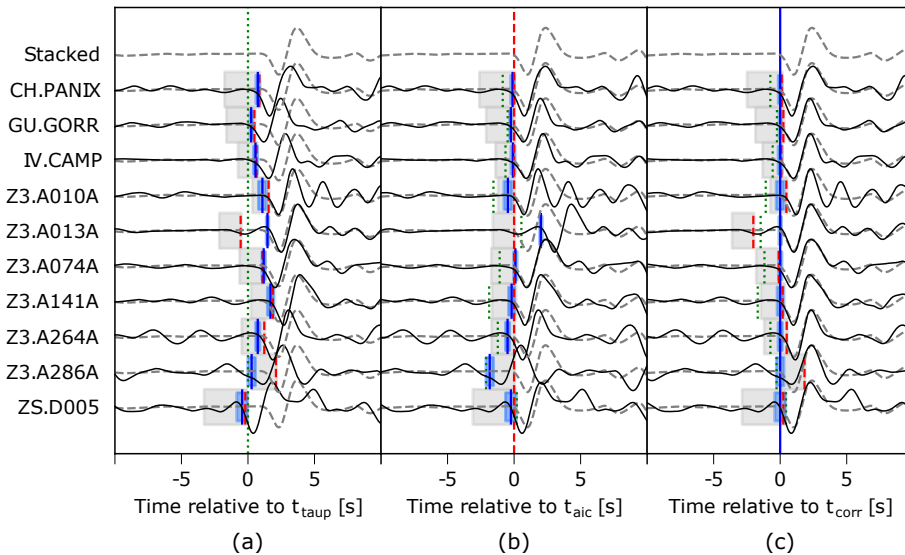
**11**

**Figure 5.** Waveform fit for P-arrivals of a M5.6 event on 7 August 2018 using the beam waveform as reference (dashed line). Left panel: Traces of different exemplary stations aligned by their theoretical onset (green dotted line). Travel time residuals (not demeaned) for each trace can be read from the differences of AIC (red dashed line) and correlation onsets (blue solid line) to the theoretical onset. Onset uncertainties are displayed by shaded areas in grey (for absolute AIC onsets) and blue colors (for relative onsets based on cross-correlation), respectively. There is a good agreement between AIC and correlation based onsets, however the estimated absolute uncertainty of the AIC onsets is large, often exceeding the residual to the theoretical onset. Middle panel: Alignment of traces by their AIC onset. Overlap with the beam trace is good, but fails in certain cases of higher noise, which can lead to too early (e.g. Z3.A013A) as well as too late (e.g. Z3.A286A) AIC onsets. Right panel: Alignment by the correlation corrected onsets. Overlap with the beam trace is close to ideal. The estimated uncertainty of correlation corrected onsets is by a factor of about 10 lower than that of the AIC picks. Note the increased uncertainty for trace ZS.D005 and Z3.A010A exhibiting significant coda.

## 3.4 Error estimation

Estimating an error for automatically determined as well as for manually assigned traveltimes is a difficult task and can be rather subjective. The concept of earliest and latest possible pick for error estimation uses information of a single trace only and is not suited for traveltime residuals determined by cross-correlation as the credibility of a time difference to a reference trace associated with a high cross-correlation coefficient is by far higher. This argument also applies for uncertainties of the absolute onsets, if the reference trace is a low-noise beam where the concept of estimating the earliest possible pick as half the signal wavelength is also questionable as the first onset may be clearly identifiable without any risk to miss the first oscillation.

As the beam represents the waveform of the majority of stations, we consider the maximum cross-correlation between station and reference trace as the most important indicator for the relative accuracy of a traveltime difference. However, this assumption only holds if the stations forming the beam trace are evenly distributed in the array and not just representing a part of the array (for example stations close to the reference station). This is vital for the consistency of the full dataset.

12

Moreover, using the cross-correlation coefficient as a measure of accuracy might lead to a down-weighting of traces of stations influenced by strong local heterogeneities whose waveform does not fit the shape of the reference trace. Fortunately, this matter can be easily identified by looking at spatial distributions of maximum correlation. Affected stations should stand out in comparison to adjacent stations when looking at correlation coefficients averaged over many events (Sect. 4). We tried to find such regional dependencies by creating spatial plots of the cross-correlation coefficient for randomly selected events, but could not find any evidence for a decrease in correlation coefficient with distance to a reference station, or any regional cluster of high or low cross-correlation coefficients.

A second criterion for a good match of station and reference trace is the shape of the cross-correlation function itself. Hence, we also evaluate the full width at half maximum (FWHM) of the cross-correlation function. If the FWHM increases, the cross-correlation maximum looses sharpness and the accuracy of a traveltime difference decreases. This approach implies a frequency dependency of traveltime uncertainty, leading to a higher uncertainty for longer periods (and hence wavelengths).

For a parabola fitted to the maximum of the cross-correlation function of the form:

$$f(x) = ax^2 + bx + c \tag{7}$$

the full width at half maximum (FWHM) can be calculated as

$$\text{FWHM} = 2\sqrt{\left(\frac{b}{2a}\right)^2 + \frac{C_{max} - 2c}{2a}}, \tag{8}$$

where $C_{max}$ denotes the maximum correlation. To combine both criteria, we chose to calculate the traveltime difference uncertainty as follows:

$$\sigma = (1 - C_{max})\,\text{FWHM} \tag{9}$$

The influence of a bad fit owing to signal coda on the cross-correlation coefficient and hence traveltime residual uncertainty is illustrated in Fig. 5c. The contribution of the width of the cross-correlation function, depending on signal period, is practically the same for all traces of this event. However, the maximum correlation decreases for stations with additional complexity in the signal (ZS.D005 and Z3.A010A).

## 4 Uncertainities of traveltime residuals

We categorize traveltime uncertainties into five different classes in steps of $0.1\,\text{s}$ ranging from class 0 (best) below $0.1\,\text{s}$ to class 4 (worst), over $0.4\,\text{s}$. Comprising over 170.000 onsets, the traveltime uncertainty distribution of $db_{0.5}$ (Fig. 6a) has a maximum at $0.08\,\text{s}$. The median of the distribution is $0.15\,\text{s}$, the mean is $0.2\,\text{s}$. Our average value of the estimated uncertainties is therefore lower than the one estimated by Lippitsch et al. (2003), who report a value of $0.36\,\text{s}$ for 4199 P-wave traveltimes and larger than the one reported by Zhao et al. (2016), who estimate a value of less than $0.1\,\text{s}$ for their 41838 traveltime residuals. However, due to the high number of stations in the AlpArray project, our dataset contains over 46.000 (27 %) of the onsets in the highest class with an estimated uncertainty $< 0.1\,\text{s}$. Less than $10\,\%$ are in the lowest class of $0.4\,\text{s}$ or higher.
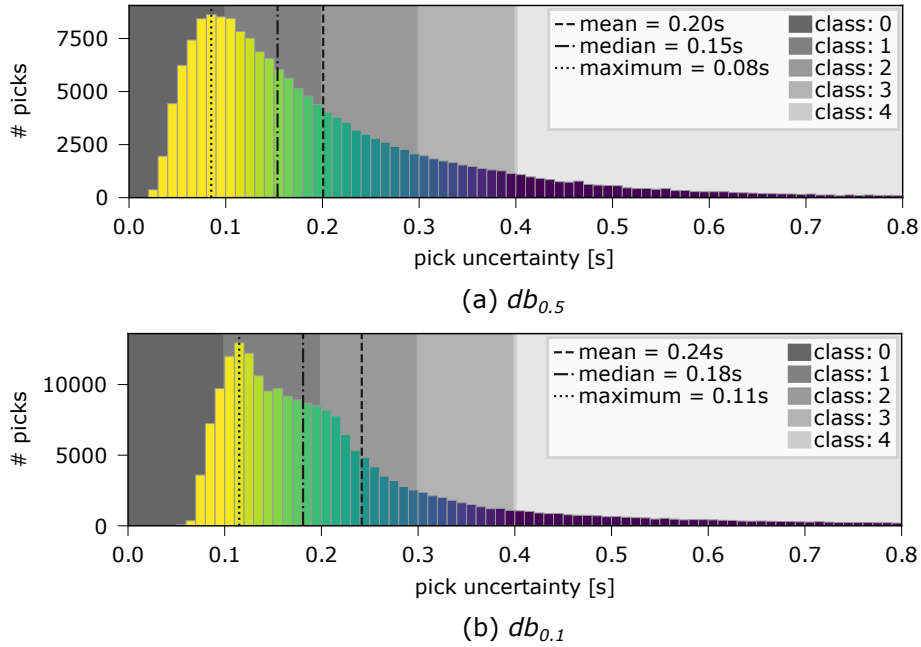
**Figure 6.** Pick uncertainty distribution of $db_{0.5}$ and $db_{0.1}$, clipped at $0.8\,$s. Uncertainties in the histograms are coloured identical to Fig. 7 for an easier comparison.

The low-frequency dataset $db_{0.1}$ has an increased signal quality (i.e. higher SNR) (Fig. 6b) which is reflected in the higher number of picks (over 214.000), an increase of over $25\,\%$ compared to the high frequency dataset. However, the traveltime uncertainty distribution is drawn to higher values, with its mean being shifted by nearly half a class towards higher uncertainties. While the peak value of the uncertainty histogram is still in the same region as that of the high frequency dataset, there are only ca. $9.8\,\%$ of the total number of picks in class 0 and over $12\,\%$ in class 4. The reason for this counter-intuitive behaviour is the fact that, owing to the greater signal periods, the maxima of the correlation function for estimating the time differences (Sect. 3.4) become wider leading to a higher error estimate.

## 4.1 Regional distribution

An evaluation of the regional distribution of the median of traveltime uncertainty per station in the $db_{0.5}$-dataset (Fig. 7a) exhibits lower values north and east of the Alpine arc, in central and southern Germany, as well as in the Czech Republic, eastern Austria and Slovenia. We hypothesize that this effect originates in the spatial segregation of those areas from the Alpine orogen, as the subsurface structure of the surrounding area of the Alps is simple in comparison to that beneath the Alps. In contrast to that, traveltime uncertainty increases above the highly complex structures in the Alpine arc, where the P-wave fronts are significantly altered by the strongly heterogeneous subsurface. This decreases their correlation with the waveforms on other stations of the array and to the stacked reference trace. It is also likely that uncertainty increases due to local site effects which can be significant in narrow valleys, where anthropogenic activities such as traffic are harder to evade. These influences

14
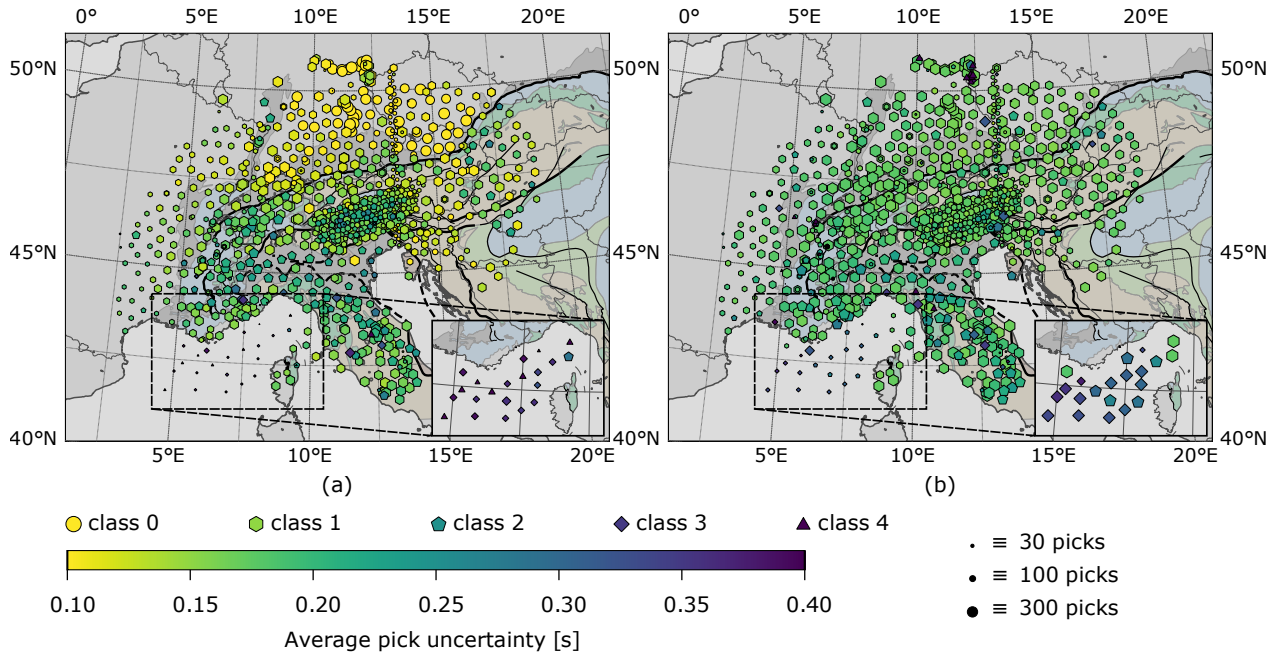
**Figure 7.** Maps of the median uncertainty of all picks for the high frequency (a) and the low frequency (b) dataset. Symbol sizes correlate with number of picks per station, color shows the average traveltime uncertainty and symbol shapes indicate the average pick class on each station. Inset shows OBS stations only with symbol size increased by a factor of 2.5. Traveltime uncertainty gets higher for $db_{0.5}$ in areas strongly influenced by deep subsurface structures, e.g. orogenic roots as well as strong heterogeneities close to the surface. Coverage in terms of measurement duration is best in the northern Alpine foreland, central Alps and Apennines. Complementary experiments are salient, as their measuring duration i.e. number of total picks is limited in contrast to other stations. The EASI experiment can be seen as a straight line of smaller sized symbols on a north-south directed profile, spatially (but with no overlap in time) cutting through the SWATH-D experiment in the central Alps above the Tauern Window. The latter has a higher station density compared to the rest of the array. Ocean Bottom Seismometers are identifiable by a lower number of picks (smaller symbol size) as well as by a higher average uncertainty as a consequence of their noisy measuring environment.

330  should be visible on single stations which show a high daytime noise level. We expect those effects to be present equally in both, the high and the low frequency dataset. However, most of the station outliers we see in one dataset is not present in the other.

The traveltime uncertainty distribution pattern of the lower frequency dataset $db_{0.1}$ (Fig. 7b) shows a shape comparable to the high frequency one with the lowest uncertainty in the northeastern parts of the array. However, overall uncertainty is higher
335  and the contrast between regions of high and low uncertainty is decreased. We assume that this is an effect of signals of larger wavelengths being less sensitive to small scale anomalies due to their lower resolution capability (finite frequency effect) and hence, waveform fit with the reference trace being easier to achieve. The only area, where we see a totally opposite behaviour is the Ligurian Sea, where the positive impact on pick uncertainty using lower frequencies is salient. Here, not only the number of

total picks greatly increased, but also average pick quality is raised by a full class for nearly all OBS, whilst for the remaining stations quality tends to decrease by almost one class in comparison to the high frequency dataset. We also note that there are only small changes in uncertainty for the SWATH-D stations. They even show slightly counterintuitive behaviour, of having higher uncertainties than average in $db_{0.5}$, but lower uncertainties than average in $db_{0.1}$.

The total number of picks per station is highest on permanent station networks, which are distributed densest in the central Alps and Apennines. Temporal coverage slightly decreases in the western part of the Array, due to a delayed start of deployment of temporary stations in this area.

## 5  Regional variation of traveltimes and traveltime residuals

In the following, we examine the variation of traveltimes and traveltime residuals across the array, study their dependence on event azimuth and in particular delve into the reproducibility and consistency of the traveltime residuals. Especially, the latter is a crucial prerequisite for a successful tomographic inversion.

### 5.1  Wave fronts and spatial patterns of traveltime residuals

We start with teleseismic P-wave fronts constructed as isolines from the estimated traveltimes. To further demonstrate the improvement of correlation-corrected traveltimes over AIC traveltimes, we show interpolated P-wave fronts constructed from both kind of traveltimes. As an example, we take the M6.5 earthquake that happened on 17 November 2017 in the Eastern Xizang-India Border Region (Fig. 8). In both cases, one can identify the P-wave traveling across the array of about 700 stations from northeast to southwest. However, when constructed from the AIC onsets (Fig. 8a), the wave fronts are strongly irregular and several outliers are apparent leading to distorted isolines which cannot be explained by mantle heterogeneities. After application of the cross-correlation correction, the resulting wave fronts do no longer show the scatter inherent to the AIC onsets and become smooth except for some weak undulations (Fig. 8b). These seem to be produced by several adjacent stations and should be attributed to subsurface structures.

To illustrate the varying shapes of the wave fronts crossing the AlpArray network from different azimuths and epicentral distances, we have selected four different earthquakes as representative examples: two with nearly equal back-azimuth ($75°$) but very different epicentral distances ($104°$ and $45°$) and two others covering western ($288°$) and southern ($218°$) back-azimuths with differing epicentral distances ($89°$ and $52°$) (Fig. 9). In addition to the P wave fronts, we show the demeaned traveltime residuals associated with each particular event as defined in eq. (1). They should correlate with the wave fronts as deformations of the wave front should lead to traveltime residuals and vice versa. To compensate influences of different station elevations, we apply a constant traveltime correction on all residuals shown, assuming vertical propagation and a surface P-wave velocity of $5.5\,\mathrm{kms}^{-1}$.

Comparing Fig. 9a and Fig. 9c reveals a notable difference of the $1\,\mathrm{s}$ traveltime isoline spacing which is much greater for the distant event. This reflects the different horizontal apparent velocity of the two wave fields which is controlled by epicentral distance and is much higher for the more distant event. While the wave fronts are generally regular and smooth,
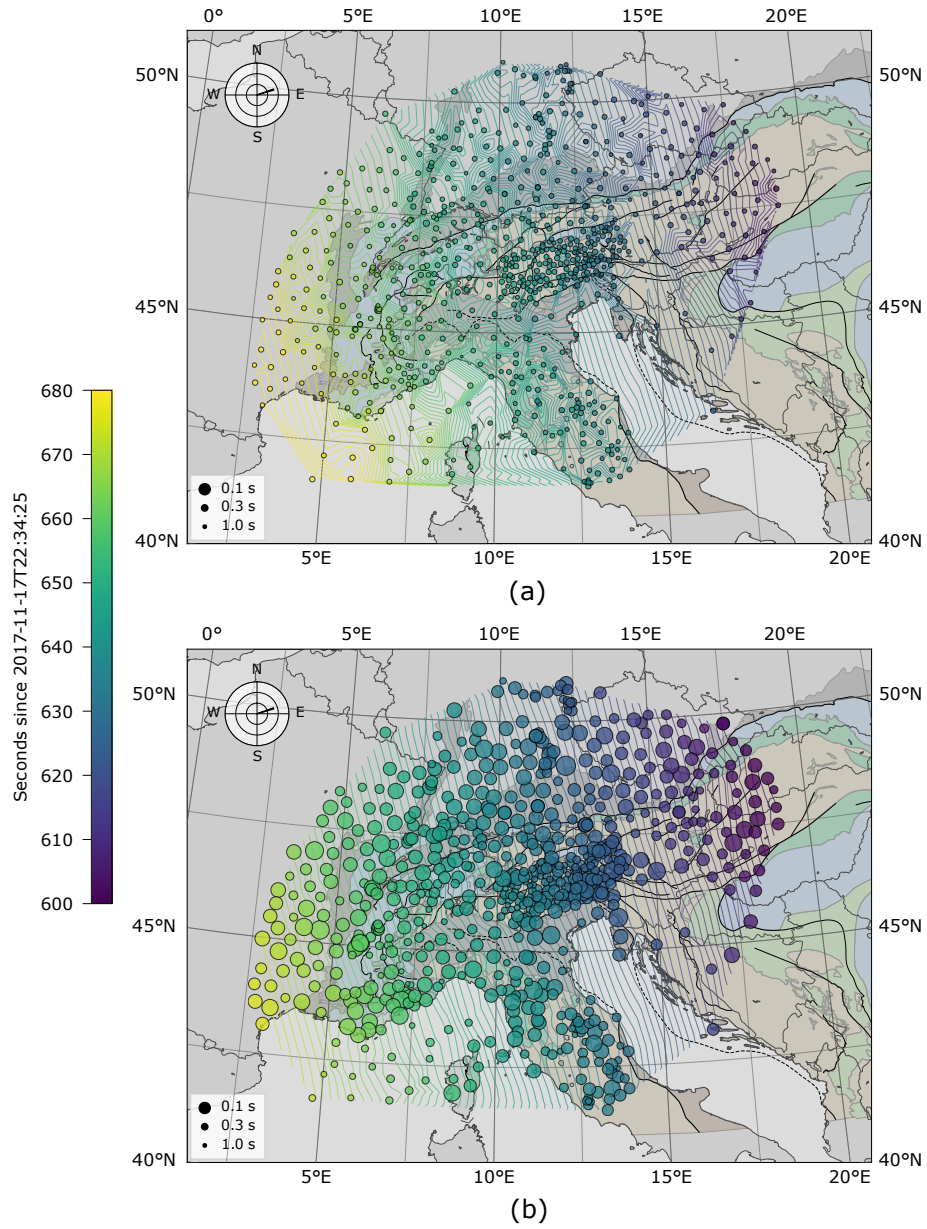
16

**Figure 8.** Traveltime fields of the Eastern Xizang-India Border Region event on 17 November 2017. Onsets from (a) the AIC algorithm that were only corrected for severe outliers (noise picks, or wrong phases) and (b) the combined cross-correlation AIC algorithm. Onset certainty increases with circle sizes. Isolines are linearly interpolated with isochrone contour intervals of 1 s.

strong distortions become visible in some places. For example, in Fig. 9a, the spacing of the isolines locally broadens in northern Italy north and east of the Ligurian Sea. This increased spacing can be associated with very large negative residuals beginning at about $7.5°E$ and $45°N$ and continuing further to the northeast. The broadening can be explained by the transition
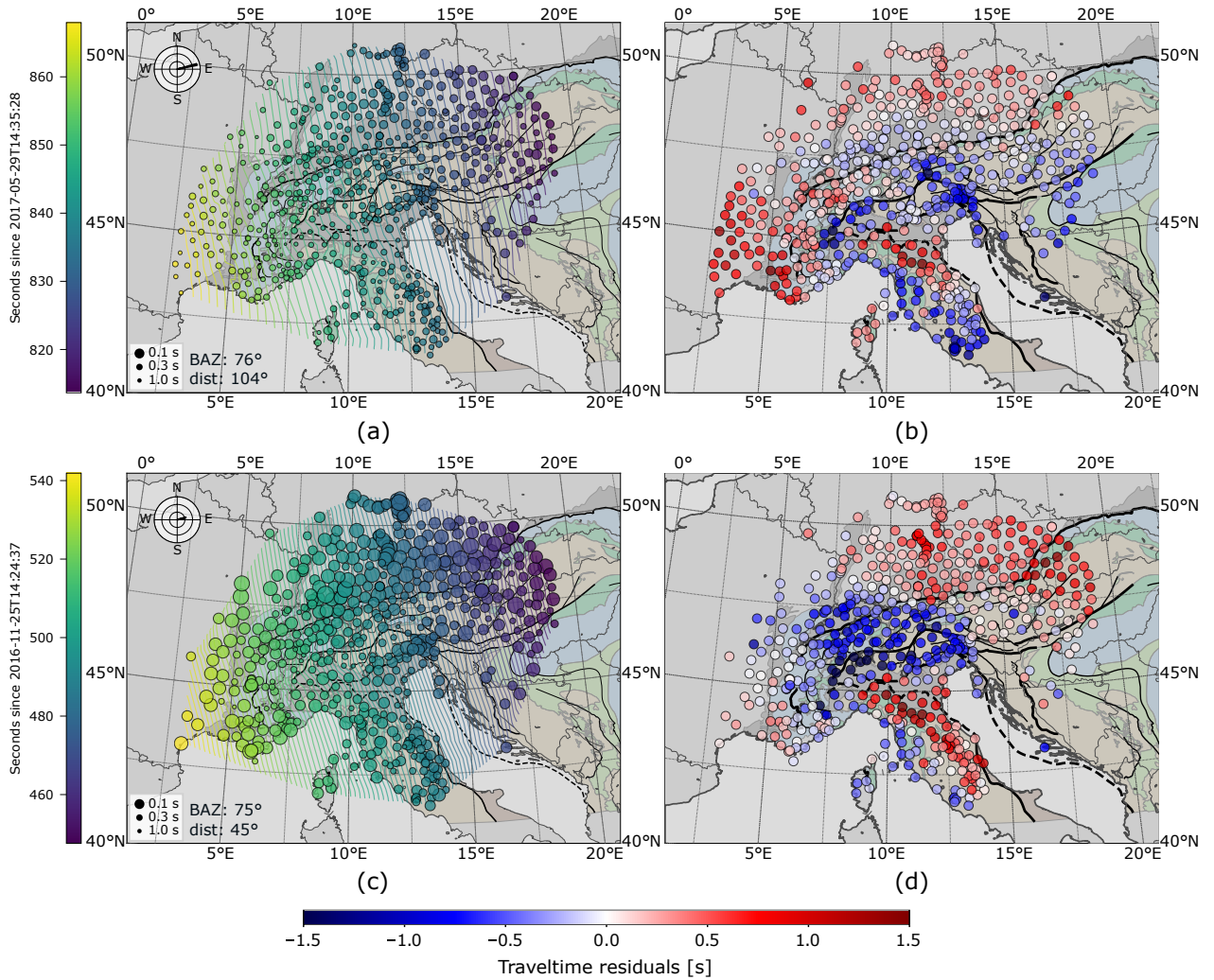
**Figure 9.** Wave fronts and traveltime residual patterns of different earthquakes. Left panel: Absolute traveltimes, distance of isolines 1 s, circle sizes inversely proportional to pick uncertainty. Right panel: Demeaned traveltime residuals relative to 1D earth model. (a), (b): M6.6 event, 2017-05-29, Sulawesi, Indonesia, BAZ=76°, distance=104°; (c), (d): M6.6 event, 2016-11-25, Tajikistan-Xinjiang Border Region, BAZ=75°, distance=45°; *Continued figure:* (e), (f): M6.8 event, 2017-06-22, Near Coast of Guatemala, BAZ=213°, distance=52°; (g), (h): M6.6 event, 2017-08-18, North of Ascension Island, BAZ=288°, distance=89°;

from normal to large negative residuals further to the southwest. A second one occurs in the Apennines to the south where the wave front has a strong lag near the western coast of Italy compared to the areas north of it but takes up again while propagating over the areas with negative residuals in the western and central Apennines. In Fig. 9c, a very similar behaviour is visible.

A closer look at the traveltime residuals, Fig. 9b and Fig. 9d, reveals that there is a general agreement between the patterns but also significant differences, for example, in southeastern France where we observe normal to negative residuals for the distant
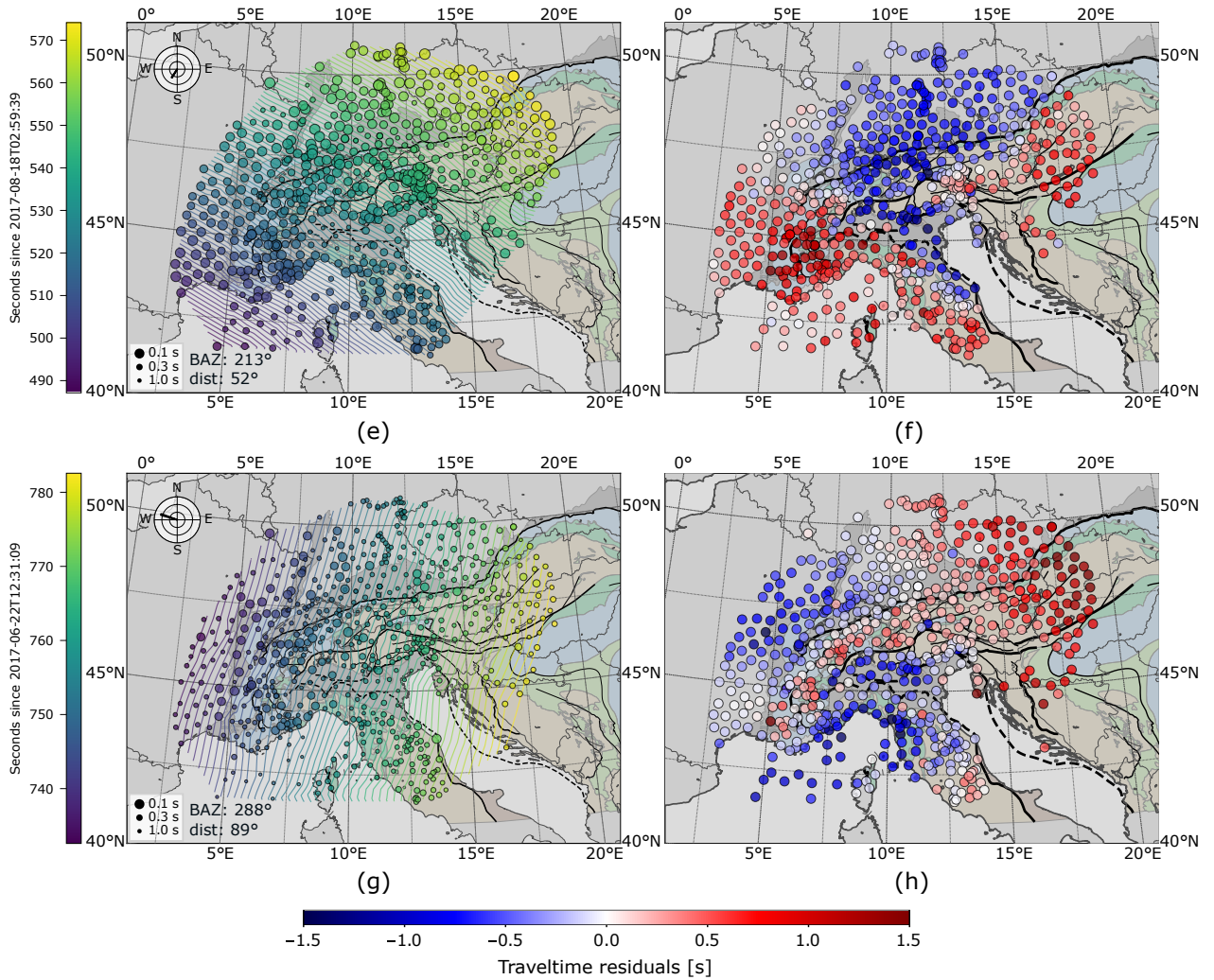
**Figure 9.** Continued.

event but positive residuals for the close event. The opposite is the case in most of Switzerland where we observe negative
380  residuals for the close event and rather normal residuals for the distant one. Apparently, the steeply upwards propagating waves
from the distant event see different subsurface structures than the more slanted waves of the close event do.

A comparable behaviour is observed for events arriving from other back-azimuths. Isoline spacing is again much larger for
the more distant event whose waves arrive from a WNW direction. In Fig. 9g, there are again notable distortions of the wave
fronts around 7.5°E and 45°N. These distortions are shifted to the NE for the waves arriving from the SSW in Fig. 9e. The
385  associated residuals exhibit large-scale coherent patterns of negative and positive residuals but are again different in various
regions. For example, residuals are generally positive in southeastern France for the waves arriving from SSW while they are

normal to negative for the event from WNW. This is again an indication of heterogeneous mantle structure to be resolved by tomography later.

## 5.2 Stacked residuals

390 Although traveltime residuals differ with epicentral distance and event back-azimuth as waves move through high or low velocity zones from different angles before reaching the surface, there are certain features which tend to occur for a large number of events. The most prominent ones are the negative residuals along the Apenninic and Alpine chain. We stacked residuals for all analysed events to identify regions of stable negative or positive traveltime residuals. It is important to understand that after stacking of the demeaned traveltime residuals, the resulting residuals are relative to an unknown one-dimensional earth model

395 defined by all events used for stacking and not to the standard earth model used to calculate traveltime differences in the first place (e.g., Aki et al., 1977). Hence, negative or positive residuals indicate higher or lower velocities, respectively, compared to this average model and not compared to a standard earth model.

As we only consider mantle phases between $35°$ and $135°$ distance, the incidence angle differs by a maximum of only $\sim 13°$ in a 1D earth model (ak135). Hence, we anticipate that the major variation of event-specific residual patterns is due to the

400 event back-azimuth and expect the influence of the incident angle on those patterns to be small in comparison. We have already noticed this when examining the different individual events (Fig. 9).

As the azimuthal distribution of the events in our database is strongly uneven (Sect. 2.1), it is important to balance out the influence of events from different directions when stacking. Otherwise, the influence of back-azimuths with high event density (e.g. NE in Fig. 2) on traveltime residuals would dominate over data from poorly covered directions. Hence, we create $30°$

405 wide back-azimuth bins and stack traveltime residuals at each station for all events reaching the station from that direction, weighted by the inverse of the uncertainty at each station. The value of $30°$ was chosen as a good compromise between angular resolution and smooth event distribution. The distribution of available measurements for different back-azimuth bin sizes can be found in the supplementary material (Fig. A1).

For an interpretation of mantle features in the residual pattern, we chose to correct the stacked residual patterns for influences

410 of the strongly heterogeneous Alpine crust. Therefore, we assembled a crustal model from different studies in the greater Alpine region, which we will show in more detail for the correction of the teleseismic traveltimes in the upcoming traveltime tomography. To create the model, we start with the generic crustal background model for Europe EuCrust-07 (Tesauro et al., 2008), which was compiled for the correction of crustal influences on seismic studies that analyse deeper structures, such as a teleseismic tomography. The layer model contains information on sediment thickness, upper and lower crustal average velocity

415 and thickness (and thus Moho depth), discretized on a $15'$ times $15'$ regular grid. It was created from various seismic reflection, refraction and receiver function studies. For the Alpine region, we improve information on the Moho depth using a more recent study of Spada et al. (2013). Lastly, for the western and central Alpine region, we replace this model with the more detailed, fully 3D regional tomographic model of Diehl et al. (2009a). We use the information on the model resolution supplied to us by T. Diehl, to assess which model to favour at a certain point in space. To only account for crustal influences in our dataset, we

420 remove velocity perturbations associated to the uppermost mantle below the suggested Moho proxy by T. Diehl of $7.25\,\mathrm{km\,s^{-1}}$.
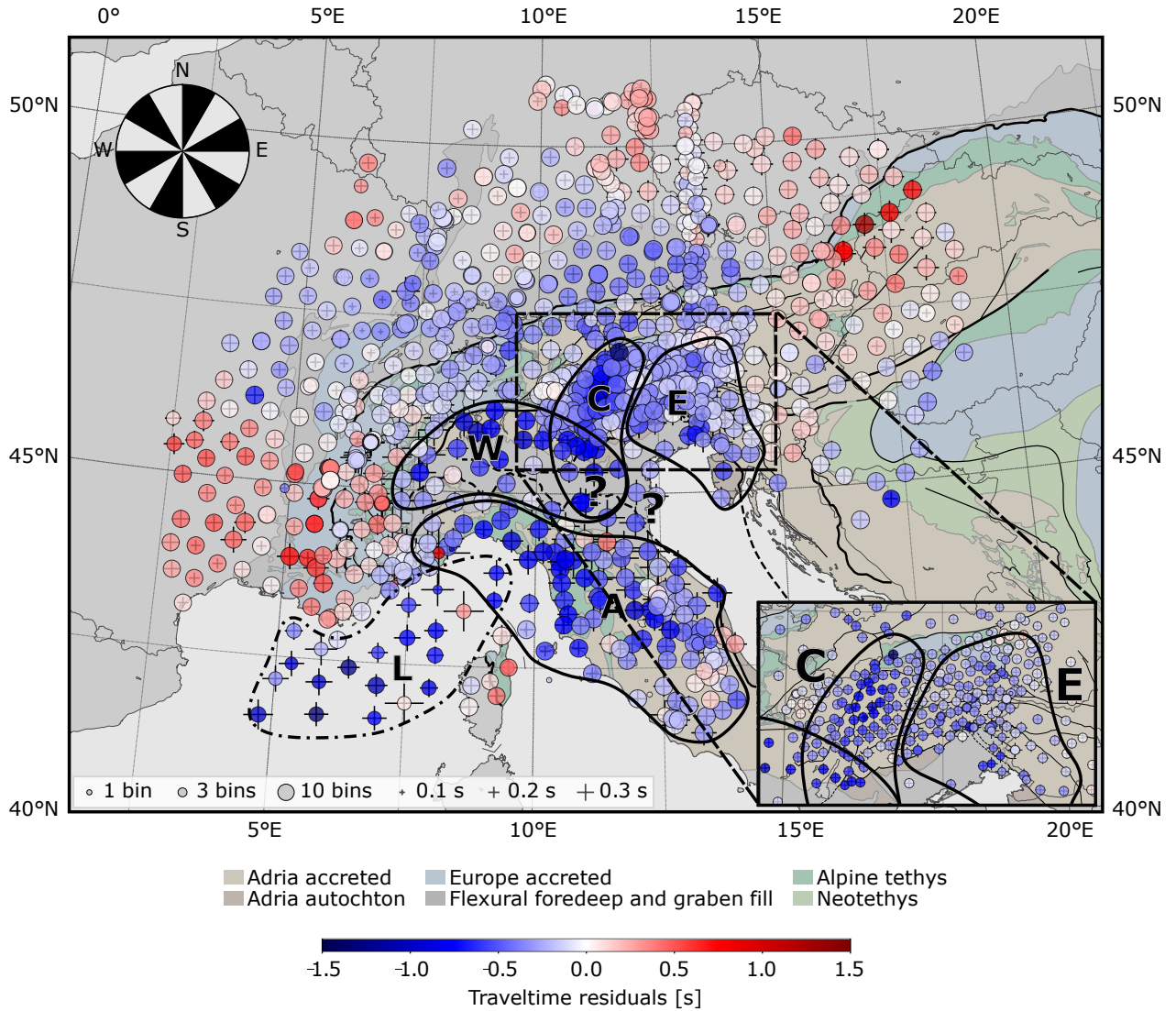
**Figure 10.** Stacked traveltime differences for 370 events of the high frequency dataset $db_{0.5}$ corrected for crustal influences. Circle sizes correlate with number of back-azimuth bins for each station (maximum = 12). Blue colors point to subsurface structures with $v_p$ values higher than average, red colors to structures with $v_p$ values lower than average. Traveltimes are binned calculating the mean traveltime for all events within $30°$ bins to balance out directional influences. Standard deviation of the azimuthal influence on each station is marked by crosses, e.g. small crosses mark stations residuals invariant to changes of the backazimuth. A traveltime correction is applied for the station elevation using a constant near-surface velocity estimate of $5.5\,\mathrm{km s}^{-1}$. High velocity anomalies contoured: W - Western Alps, C - Central Alps, E - Eastern Alps, A - Apennines, L - Ligurian Basin. Tectonic map of the Alpine chains compiled by M.R. Handy

The resulting, vertically stacked traveltime differences (assuming a planar, vertically incident wave front) to the minimum 1D model for the Alps by Diehl et al. can be found in Fig. A2 in the supplementary material.

The most striking features of the stacked traveltime residuals are the negative residuals following the Alpine arc from 45°N, 7.5°E to 46°N, 14.5°E (Fig. 10). We subdivide those anomalies into three major parts that can be related to presumed slab remnants in the upper mantle. The western negative anomaly (W) can be clearly differentiated from a large zone of positive residuals to the west. It follows the Alpine mountain chain to the east, bending south towards the Po-plain. The central negative anomaly C is attached to anomaly W in the south but follows a very different strike indicating a lateral change in mantle structure. Defining a separate negative anomaly in the Eastern Alps (E) bending circular to the south towards the Dinarides is not that obvious but substantiated by the observations in the even denser SWATH-D array (see inset in Fig. 10) which indicate a narrow gap of close to zero residuals between C and E. This finding points to another discontinuous lateral change of mantle structure below.

## 5.3 Azimuthal dependence

We already showed traveltime residuals for individual wave fields. To give a more stable impression of the azimuthal variation of the residuals, we stacked 3 neighbouring 30° averages to cover the four major azimuthal sectors NE, SE, SW and NW (Fig. 11). All of them exhibit the negative residuals following the Apennine and the Alpine chain, the generally normal-to-negative residuals in the northern foreland, the generally normal-to-positive residuals in southeastern France and the Pannonian basin. However, we notice that the residual anomalies move around depending on the major azimuthal direction. We have roughly sketched the positions of the five negative residuals that we already presented in Fig. 10 to investigate how the residuals move laterally when illuminated from different directions.

To draw some first conclusions on the possible location of structures forming the residual pattern, we imagine a planar wave front propagating through the subsurface from each of the four major azimuthal quadrants, creating an imprint of the traveltime residuals it accumulated on its way to the surface. Due to wave refraction, the propagation direction of the wave fronts is almost vertical close to the surface, whereas for greater depths the incidence angle increases. It follows that residual patterns that persist for all four major azimuths point to structures located closer to the surface. Features shifting laterally when illuminated from different directions suggest structures that are located at greater depths. If a feature in the residual pattern can not be recovered at all from another direction it is likely to be related to a very deep anomaly that lies outside the overlapping area of the ascending seismic waves. However, it is always possible that the effect of one anomaly is removed, or enhanced by superposition with another.

A good example for a structure with a laterally moving imprint is the Apenninic anomaly (A) that we find at the western Italian coast penetrating into central Italy with a strike of 130°. When illuminated from the northeast (Fig. 11a), the negative traveltime residuals tend to move to the southwest and can even be tracked by the OBS stations off the Italian coast. Looking at the same anomaly illuminated from the southwest (Fig. 11c), we see that its imprint moves to the northeast and into the Adriatic Sea where we loose its track due to missing seismological stations. Illuminating the structure from perpendicular directions (Fig. 11b and d), the resulting pattern of negative residuals remains mostly the same.

Another remarkable difference to the stacked traveltime perturbation pattern from all azimuths can be seen in the imprints of structure (C) and (E) between 12°E and 15°E. Both show very strong negative traveltime residuals that can not be separated
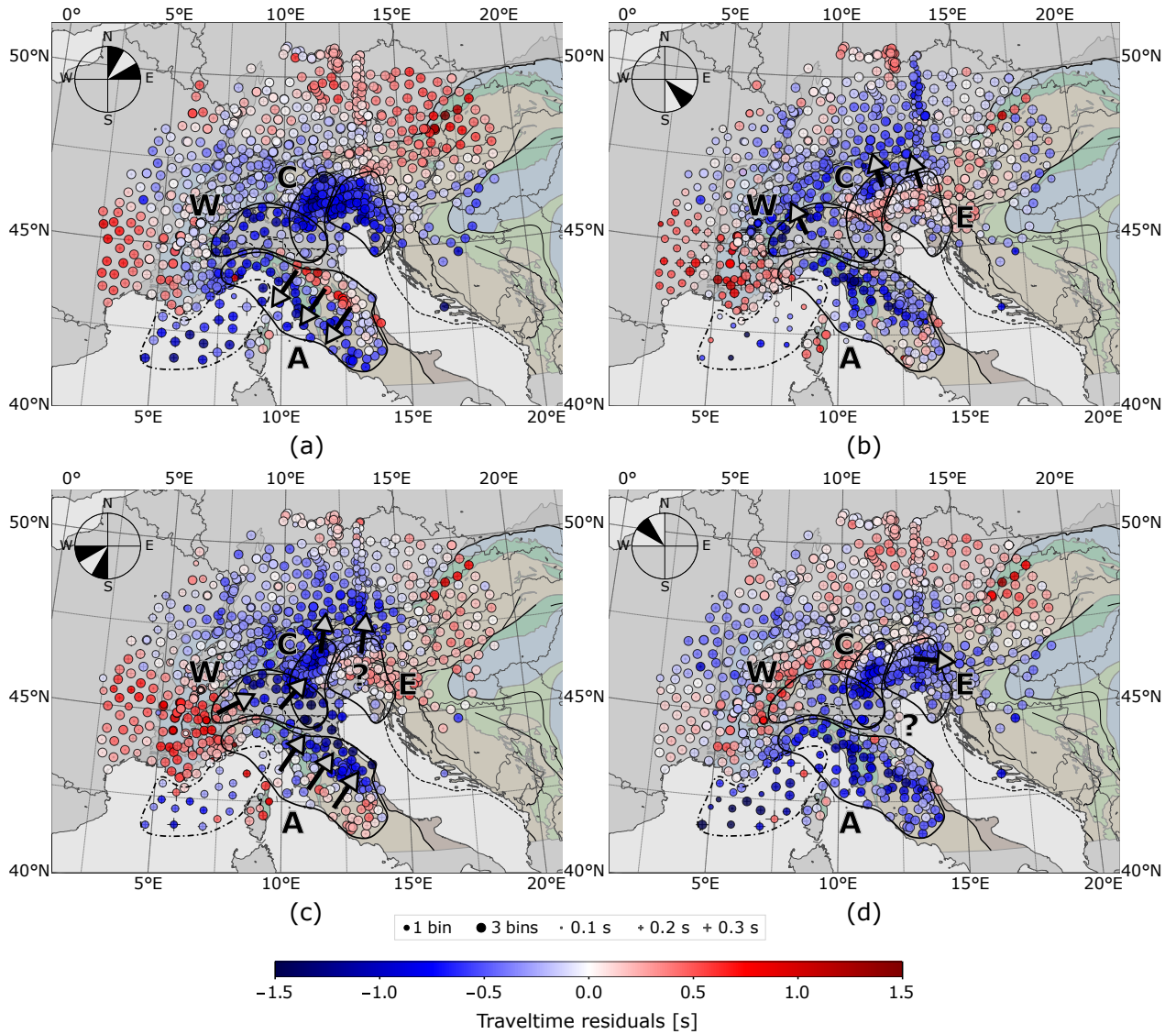
**Figure 11.** Traveltime residuals stacked for $90°$ quadrants NE, SE, SW, NW. For each quadrant the traveltime average of three possible $30°$ bins is shown. Circles of stations with incomplete coverage appear smaller; e.g. in (b): several directions are missing for OBS from SE direction, which has lowest event coverage. Dashed lines show outlines of the same negative residual anomalies as in Fig. 10. Arrows indicate a lateral movement of anomaly imprints caused by an illumination of waves of different azimuths.

into two parts when illuminated from the northeast (Fig 11a). These residuals do not appear with the same intensity for other azimuths, which is an indication of a northeast dipping of the corresponding high-velocity anomalies. The reason is that waves incident from northeast may accumulate a large negative traveltime residual while waves incident from other directions acquire only minor changes in traveltime. Illuminated from the southwestern direction, (Fig 11c) we see that only the imprint of the

460

23

western anomaly (C) remains. Looking at the same anomalies from the northwest, (Fig 11d), we see again the imprint of structure (C) but with a lower amplitude and a possible imprint of a deeper part of structure (E) that is shifted to the east. The high velocity anomaly building (C) might therefore be dipping more vertically with less extension into the mantle, but with a stronger positive velocity perturbation. Illuminated from the southeast, (Fig 11b), we see again a strong negative residual of structure (C) that is probably superimposed on a deeper part of structure (W). The negative residuals of anomaly (E) almost completely disappear within the drawn outline. Here, we again see that most of structure (E) as well a a large part of structure (C) seem to have been shifted to the northwest, indicating great depths of the underlying anomalies.

The western Alpine anomaly (W) shows negative residuals illuminated from the southeast that are smeared to the northwest(Fig 11b) and shows only moderate negative residuals illuminated from the opposite direction. This indicates a dipping of structure (W) to the southeast.

## 5.4 Frequency dependence

Up to now not much was said about the low-frequency dataset with maximum frequency $0.1\,$Hz which we assembled owing to the high noise on the OBS records in the higher frequency band. As for the $0.5\,$Hz-dataset, we determined absolute traveltimes and traveltime residuals using the techniques described above. We find that the obtained maps of traveltime residuals differ systematically between the considered frequencies.

Physical reasons for a frequency dependence of traveltime residuals estimated by cross-correlation can be dispersion due to attenuation (Liu et al., 1976) or the fact that the interaction of seismic waves with heterogeneous structures depends on wavelength and hence also on frequency. The former describes the fact that the velocity of waves in attenuating media becomes frequency dependent while the latter leads to deviations from predictions of ray theory which is a zero-wavelength approximation. It is often referred to as the finite-frequency effect with wave front healing (Wielandt, 1987) as one prominent example. One may also suspect that the applied low-pass filter may affect the traveltime residuals as the group delay of the filter increases with decreasing corner frequency. However, assuming that all travel times at the lower frequency $f_1$ are delayed relative to those at the higher frequency $f_2$ by $\Delta\tau$ implies that also the array averages are delayed by $\Delta\tau$. Since we subtract the array average the delay cancels making the demeaned residual filter independent. Thus, frequency dependence of the traveltime residuals should be explained by the physical reasons mentioned above.

To illustrate the differences between both frequency bands, we directly show traveltime residuals determined for the $0.1\,$Hz dataset (Fig. 12a), and we form differences of the traveltime residuals, i.e. we subtract the values for the low-frequency dataset from those of the high-frequency dataset (Fig. 12b).

Both are stacked in $30°$ bins as well, similar to the high frequency dataset, to account for the uneven azimuthal distribution. The residuals of $db_{0.1}$ (Fig. 12a) are also corrected for the crustal influence. At first glance, there are no striking differences between residuals of $db_{0.5}$ (Fig. 10) and $db_{0.1}$ (Fig. 12a). Both show very similar patterns of negative and positive residuals. However, when taking a closer look we see that the negative residuals of the $0.1\,$Hz dataset seem less strong and less well-defined around the central (C) and eastern (E) anomaly. In contrast to that, we see a marked increase in amplitude of the negative residuals in the Po-plain.

The differences between the stacked residuals for the $0.5\,\text{Hz}$ and the $0.1\,\text{Hz}$ dataset (Fig. 12b) show coherent regions of positive and negative disparity with the negative ones in the region of anomalies C and E as well as the southeastern part of A and a positive one in the area of the Po-plain between anomalies W and A. We assume that these disparities are caused by the finite-frequency effect, because low frequency waves ($0.1\,\text{Hz}$) and their traveltimes are less influenced by both, high-velocity anomalies beneath C and E and the only few kilometer thick low P-wave velocity sediments in the Po-plain, compared to the high frequency waves at $0.5\,\text{Hz}$. Thus, residuals at $0.1\,\text{Hz}$ are less negative than at $0.5\,\text{Hz}$ for high-velocity heterogeneities leading to a negative disparity, and less positive than at $0.5\,\text{Hz}$ for low-velocity heterogeneities, leading to a positive disparity. This effect leads to an overestimation of negative residuals in the Po-plain after crustal correction, as our simple crustal correction approach does not account for the finite-frequency effect.

On the contrary, dispersion due to attenuation would produce a very different effect. According to Liu et al. (1976), high frequency waves should travel increasingly faster compared to low-frequency ones with increasing attenuation. Thus, over regions of high velocities with potentially low attenuation frequency disparity should be close to zero. Moreover, over low velocity regions with potentially high attenuation we would expect a negative frequency disparity. Both tendencies are opposite to what we observe. In the remaining regions, deviations are rather small with a weak tendency to negative values especially in the Alpine foreland.

There is a massive increase in the total number of picks for the ocean bottom seismometers, which reflects the increase in onsets and onset quality we could see in Sect. 4. Also the standard deviation of residuals with backazimuth is lower for the OBS, because there are more picks available, even from the poorly covered backazimuths. The number of OBS picks for all events increases from $421$ to $1113$ ($+164\,\%$), compared to a $25\,\%$ increase only for all stations. This might have a notable effect on resolving structures below the Ligurian Sea when performing a teleseismic tomography. In the case of our stacked traveltime residuals, we do not see a strong effect, because most of what we could see balances out by the azimuthal binning.

## 6 Discussion

With large and dense arrays like AlpArray the amount of available records for traveltime measurements may readily accumulate to hundreds of thousands depending on the duration of the deployment. Hence, automatic procedures for determining traveltimes become mandatory. Moreover, with higher resolution capabilities of such arrays, also demands on the accuracy of traveltimes have increased, in particular if we want to resolve the correspondingly small travel time differences between nearby stations. Sophisticated automatic picking procedures apparently do not meet these demands. To overcome this problem, measurements of relative time shifts between two traces by cross-correlation can be used. They can be automated and are particularly well suited for dense arrays which provide a wealth of similar waveforms. However, they do not provide absolute traveltimes. For this reason, stacking or beamforming to obtain stable low-noise reference traces is an essential further element in traveltime determination (Rawlinson and Kennett, 2004). Mitterbauer et al. (2011) already used such an approach in their teleseismic tomography of the eastern Alps even though they only determined about 6600 traveltimes. They stacked records aligned to automatic picks to obtain low-noise reference traces for ensuing cross-correlation measurements. After determining
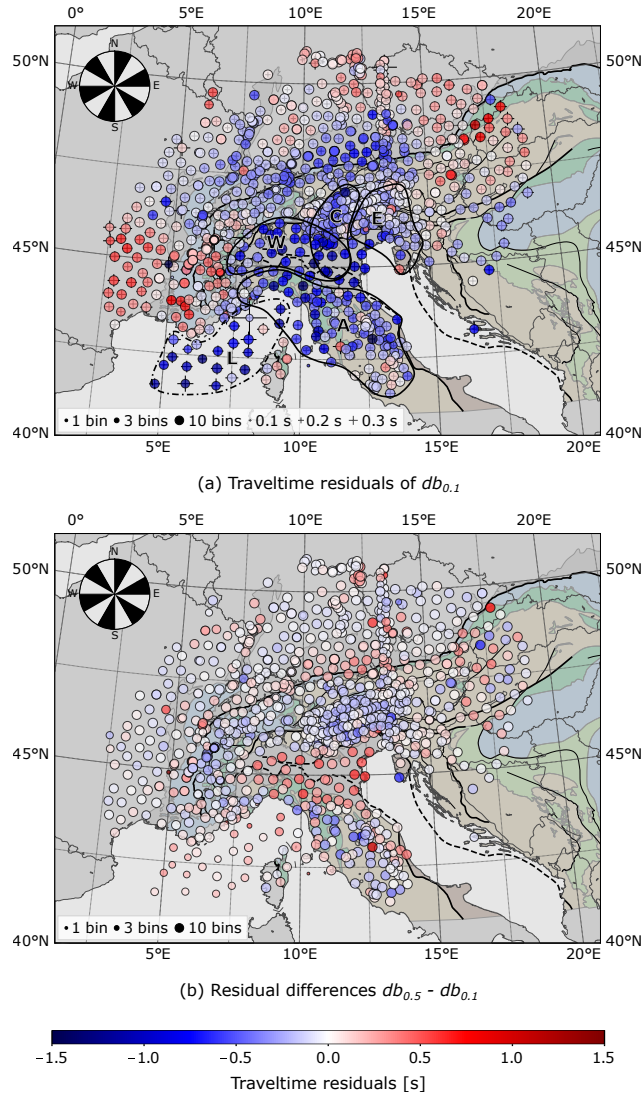
**Figure 12.** (a): Stacked traveltime residuals for $30°$ bins from all directions for $db_{0.1}$ similar to Fig. 10. Patterns look similar in most areas to the one for the high frequency dataset at first glance, except for weaker residual amplitudes. (b): Differences between stacked residuals of high and low frequency datasets show areas with positive disparity (e.g. Po-plain), or negative disparity (e.g. Apennines, Alpine arc). Proportion of pick differences (same ray available in each dataset) to total number of picks in $db_{0.5}$ is 96 %.

cross-correlation time-shifts they iterated the correlation and stacking step until a stable reference trace was obtained. Our approach is similar to that of Mitterbauer et al. (2011), as it also makes use of the elements automatic picking, beamforming

530  and cross-correlation. These are absolutely essential to obtain the required accuracy. But we found that iterative correlation and stacking was not necessary with AlpArray data, neither for the $0.5\,\mathrm{Hz}$ nor the $0.1\,\mathrm{Hz}$ dataset. It proved sufficient to select one centrally located permanent station and correlate its waveform with the waveforms of all other stations to obtain time-shifts

for constructing a stable and very-low noise reference or beam trace. Picking this beam trace automatically and using it as a reference trace for cross-correlation time-shift measurements was sufficient to obtain highly accurate relative and absolute traveltimes for up to 210.000 records in a fully automated fashion.

The uncertainty of a cross-correlation time delay measurement is evidently related to the width of the maximum of the cross-correlation function where the time delay is read off. We measure the full width at half maximum (FHWM) which is however a too conservative estimate of the real error. For this reason, we include the maximum normalised correlation $C_{max}$ as a second component into error estimation. The higher the maximum correlation the better is the delay time estimate. We reflect this expectation by scaling the FHWM by a factor of $1 - C_{max}$. This definition nicely includes the frequency dependence of uncertainty with a higher error at low frequencies because the signal gets smoother and onsets more emerging. In addition, it allows a consistent and automatic determination of uncertainty. Our reconstructions of smooth and nearly unperturbed wave fronts across the entire array from the observed travel time field with wave fronts separated by only 1 second of traveltime demonstrate that the estimated traveltime uncertainties of on average $0.2$ s (median $0.15$ s) is realistic since otherwise conspicuous bumps should appear in the wave fronts, as they indeed do when the wave fronts are constructed from the automatic picks. Further evidence for the consistency and accuracy of the estimated traveltimes and traveltime residuals are the coherent and reproducible maps of traveltime residuals obtained for individual events which correlate well with undulations of the reconstructed wave fronts.

We do not perform a tomographic inversion of the dataset here (which will be presented in a follow-up paper) but the maps of residual traveltimes already allow some inferences on the underlying mantle heterogeneities. Especially the maps of stacked residuals reflect robust spatial patterns of anomalies that occur in most of the event-specific residual traveltime maps. Most remarkable are here the negative traveltime anomalies designated with the letters L, A, W, C and E in Fig. 10. The anomaly L in the Ligurian Sea apparently reflects thin oceanic crust underlain by high-reaching fast upper mantle leading to a reduction of travel times. The anomaly A strikes with the Apenninic mountain chain, forming a narrow band along the western Italian coast in the north and then opening up into a broad band below central Italy. It indicates slab-like high-velocity mantle material beneath the Appennines. The slab seems to dip nearly vertically since the negative traveltime anomalies are systematically offset to the southwest (northeast) for waves arriving from the northeast (southwest) (Fig. 11). The anomaly W apparently reflects the generally southeast dipping subduction of European lithosphere in the Western Alps as previously inferred by Lippitsch et al. (2003). The lateral continuity of this anomaly ends at the transition from the Western to the Eastern Alps at about 10 degrees east where we find anomaly C which exhibits a very different strike. A further lateral transition to anomaly E seems to occur at about 12 degrees east at the western rim of the Tauern window.

It is of course not possible to infer mantle structure just from the stacked traveltime residuals because they integrate over depth. This problem can only be solved by a tomographic inversion of the event-specific residual maps. Nevertheless, we can already recognize prior to an inversion that slab structure underneath the Alps is complicated and high-velocity structures do not form laterally coherent bodies along the Alpine chain. This laterally discontinuous behaviour of the traveltime residuals matches previous findings by Lippitsch et al. (2003) and Mitterbauer et al. (2011) who identified different lateral slab segments in the western, central and eastern Alps with possible changes in slab dip. In particular, the slab structure belonging to anomaly

**27**

(E) is disputed because Lippitsch et al. (2003) favor a north-dipping slab while Mitterbauer et al. (2011) infer a nearly vertical slab. An amplification of the negative traveltime residuals when illuminating the structure from northeast compared to other azimuths favors a northeastern dipping structure, as we could see in Fig. 11. Due to the complexity of the region, however, it is essential to carry out a complete teleseismic tomography in order to obtain more precise information about the geometry.

Another interesting aspect of our traveltime measurements is their frequency dependence, in particular the differences between the traveltime residuals derived from the $0.5\,\text{Hz}$ and the $0.1\,\text{Hz}$ dataset. They are most probably due to the finite-frequency effect because dispersion due to attenuation predicts disparity patterns which are inconsistent with the observations.

## 7   Conclusions

The dense AlpArray Seismic Network and its complementary deployments offer the unique opportunity to infer mantle structure beneath the greater Alpine region with an unprecedented resolution. However, to benefit fully from the array, absolute traveltimes and traveltime residuals of high accuracy and consistency are required. We have shown that even very sophisticated automatic picking algorithms based on higher-order statistics and the Akaike information criterium are unable to fulfill this requirement. We demonstrate that, instead, a hybrid approach combining characteristic function picking, waveform cross-correlation and beamforming techniques that takes advantage of the dense array is indeed capable of achieving the required accuracy. Since this hybrid approach is also fully automated, human effort is drastically reduced and the consistency of the generated dataset is ensured by the reproducibility of the automatically determined onsets. Beamforming requires similar waveforms posing demands on array density depending on frequency range. AlpArray proved to be sufficient for high correlation at the chosen lowpass filter frequencies ($0.5\,\text{Hz}$ and $0.1\,\text{Hz}$). Admitting higher frequencies may require smaller interstation distances to preserve waveform coherency.

The accuracy of traveltimes and residuals is validated by the fact that they allow a reliable and flawless construction of teleseismic wave fronts in terms of traveltime isochrons. These exhibit small undulations indicating the presence of mantle heterogeneities. The traveltime residuals for individual events show very coherent and reproducible spatial patterns that perfectly fit to these undulations and, although masked by their dependence on illumination incidence and azimuth, already give a glimpse on mantle velocity anomalies, in particular conspicuous slab-like high velocity structures along the Alpine arc and the Apennines. Studying the azimuthal variations of the residuals provides first hints on the dip of these anomalies. Even stacks of residuals maps from hundreds of events show distinct, spatially coherent areas of positive and negative residuals and, in particular, reproduce the conspicuous negative residuals. These results indicate the stable presence of mantle heterogeneities in each map of traveltime residuals and allow us to make assertions about the geometry and position of the high and low-velocity objects below the Alps even before performing a full teleseismic tomography.

Maps of traveltime residuals derived from data filtered to different maximum frequencies show similar patterns but are different with respect to amplitude and sharpness of the anomalies confirming that the sensitivity of waves to heterogeneities depends on wavelength. Hence, datasets of traveltime and residuals obtained from differently filtered waveforms can not be used together in a classical traveltime tomography.
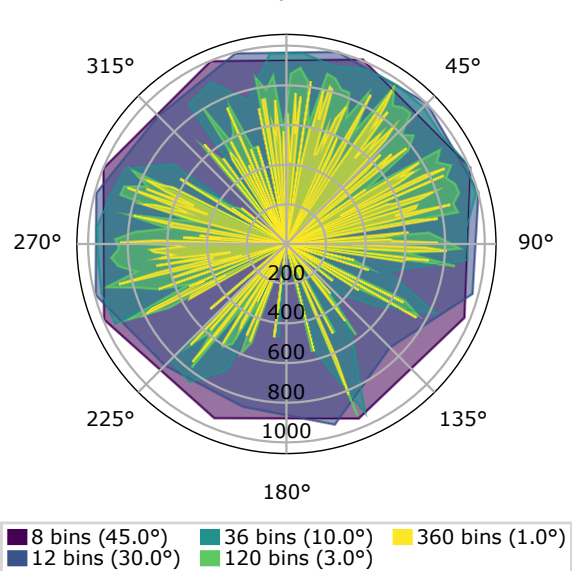
28

**Figure A1.** Number of stations for each bin for different bin sizes. Distribution is rather homogeneous for $30°$ and $45°$ bins. With smaller bin sizes bias increases, which downweights back-azimuths with low event coverage.
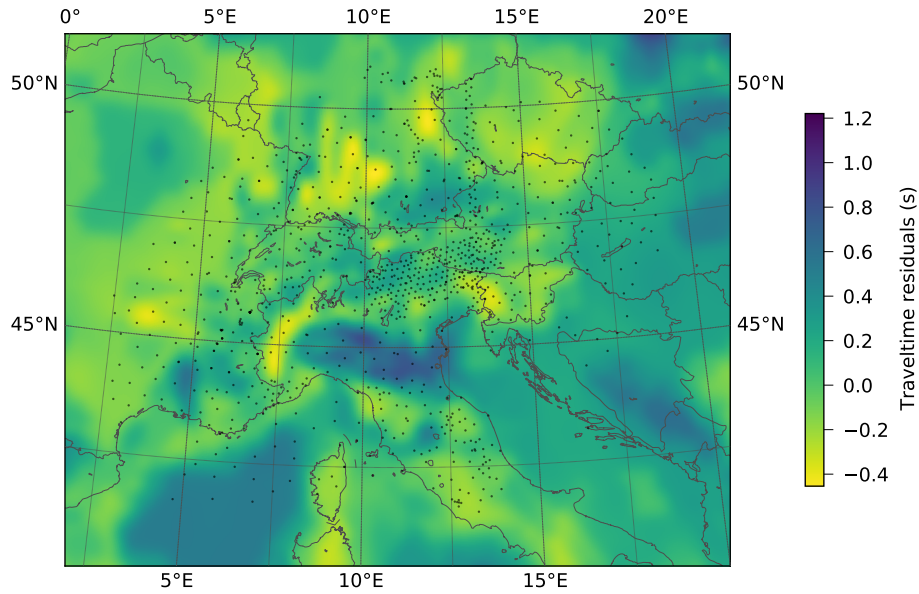
**Figure A2.** Vertically stacked traveltime residuals of crustal model compared to reference minimum 1D model of Diehl et al. (2009a). The most prominent features are the high-velocity anomaly in the western Alps (Ivrea body) and the low-velocity anomaly of the Po-plain. Low-velocities of Molasse sediments are compensated by higher velocities in the crust of the Diehl model.

*Team list.* The AlpArray Seismic Network team: György HETÉNYI, Rafael ABREU, Ivo ALLEGRETTI, Maria-Theresia APOLONER, Coralie AUBERT, Simon BESANÇON, Maxime BÈS DE BERC, Götz BOKELMANN, Didier BRUNEL, Marco CAPELLO, Martina ČARMAN, Adriano CAVALIERE, Jérôme CHÈZE, Claudio CHIARABBA, John CLINTON, Glenn COUGOULAT, Wayne C. CRAW-
605 FORD, Luigia CRISTIANO, Tibor CZIFRA, Ezio D'ALEMA, Stefania DANESI, Romuald DANIEL, Anke DANNOWSKI, Iva DASO-
VIĆ, Anne DESCHAMPS, Jean-Xavier DESSA, Cécile DOUBRE, Sven EGDORF, ETHZ-SED Electronics Lab, Tomislav FIKET, Kasper FISCHER, Florian FUCHS, Sigward FUNKE, Domenico GIARDINI, Aladino GOVONI, Zoltán GRÁCZER, Gidera GRÖSCHL, Stefan HEIMERS, Ben HEIT, Davorka HERAK, Marijan HERAK, Johann HUBER, Dejan JARIĆ, Petr JEDLIČKA, Yan JIA, Hélène JUND, Edi KISSLING, Stefan KLINGEN, Bernhard KLOTZ, Petr KOLÍNSKÝ, Heidrun KOPP, Michael KORN, Josef KOTEK, Lothar KÜHNE, Krešo
610 KUK, Dietrich LANGE, Jürgen LOOS, Sara LOVATI, Deny MALENGROS, Lucia MARGHERITI, Christophe MARON, Xavier MARTIN, Marco MASSA, Francesco MAZZARINI, Thomas MEIER, Laurent MÉTRAL, Irene MOLINARI, Milena MORETTI, Anna NARDI, Jurij PAHOR, Anne PAUL, Catherine PÉQUEGNAT, Daniel PETERSEN, Damiano PESARESI, Davide PICCININI, Claudia PIROMALLO, Thomas PLENEFISCH, Jaroslava PLOMEROVÁ, Silvia PONDRELLI, Snježan PREVOLNIK, Roman RACINE, Marc RÉGNIER, Miriam REISS, Joachim RITTER, Georg RÜMPKER, Simone SALIMBENI, Marco SANTULIN, Werner SCHERER, Sven SCHIPPKUS, Detlef
615 SCHULTE-KORTNACK, Vesna ŠIPKA, Stefano SOLARINO, Daniele SPALLAROSSA, Kathrin SPIEKER, Josip STIPČEVIĆ, Angelo STROLLO, Bálint SÜLE, Gyöngyvér SZANYI, Eszter SZŰCS, Christine THOMAS, Martin THORWART, Frederik TILMANN, Stefan UEDING, Massimiliano VALLOCCHIA, Luděk VECSEY, René VOIGT, Joachim WASSERMANN, Zoltán WÉBER, Christian WEIDLE, Viktor WESZTERGOM, Gauthier WEYLAND, Stefan WIEMER, Felix WOLF, David WOLYNIEC, Thomas ZIEKE, Mladen ŽIVČIĆ, He-lena ŽLEBČÍKOVÁ. The AlpArray SWATH-D field team: Luigia Cristiano (Freie Universität Berlin, Helmholtz-Zentrum Potsdam Deutsches
620 GeoForschungsZentrum (GFZ), Peter Pilz, Camilla Cattania, Francesco Maccaferri, Angelo Strollo, Günter Asch, Peter Wigger, James

**30**

*Author contributions.* Wolfgang Friederich developed the initial idea of the project. Marcel Paffrath developed the code and ran the calculations. Marcel Paffrath prepared the article with contributions from Wolfgang Friederich.

*Competing interests.* The authors declare that they have no conflict of interest.

# References

Akaike, H.: Autoregressive model fitting for control, Annals of the Institute of Statistical Mathematics, 23, 163–180, https://doi.org/10.1007/BF02479221, 1971.

Akaike, H.: A new look at the statistical model identification, IEEE transactions on automatic control, 19, 716–723, 1974.

665    Aki, K., Christoffersson, A., and Husebye, E. S.: Determination of the three-dimensional seismic structure of the lithosphere, Journal of Geophysical Research (1896-1977), 82, 277–296, https://doi.org/10.1029/JB082i002p00277, 1977.

Albuquerque Seismological Laboratory (ASL)/USGS: Global Seismograph Network (GSN - IRIS/USGS), https://doi.org/10.7914/SN/IU, 1988.

Allen, R.: Automatic phase pickers: Their present use and future prospects, Bulletin of the Seismological Society of America, 72, S225–S242,
670    1982.

Allen, R. V.: Automatic earthquake recognition and timing from single traces, Bulletin of the Seismological Society of America, 68, 1521–1532, 1978.

AlpArray Seismic Network: AlpArray Seismic Network (AASN) temporary component, AlpArray Working Group, Other/Seismic Network, doi, 10, 2015.

675    Baer, M. and Kradolfer, U.: An automatic phase picker for local and teleseismic events, Bulletin of the Seismological Society of America, 77, 1437–1445, 1987.

Butzer, S., Kurzmann, A., and Bohlen, T.: 3D elastic full-waveform inversion of small-scale heterogeneities in transmission geometry, Geophysical Prospecting, 61, 1238–1251, 2013.

CERN: CERN Seismic Network, 2017.

680    Deichmann, N. and Garcia-Fernandez, M.: Rupture geometry from high-precision relative hypocentre locations of microearthquake clusters, Geophysical Journal International, 110, 501–517, https://doi.org/10.1111/j.1365-246X.1992.tb02088.x, 1992.

Department Of Earth And Environmental Sciences, Geophysical Observatory, University Of Munchen: BayernNetz, https://doi.org/10.7914/SN/BW, 2001.

Deschamps, A. and Beucler, E.: POSA experiment, https://doi.org/10.15778/RESIF.ZH2016, 2013.

685    Diehl, T., Husen, S., Kissling, E., and Deichmann, N.: High-resolution 3-D P-wave model of the Alpine crust, Geophysical Journal International - GEOPHYS J INT, 179, 1133–1147, https://doi.org/10.1111/j.1365-246X.2009.04331.x, 2009a.

Diehl, T., Kissling, E., Husen, S., and Aldersons, F.: Consistent phase picking for regional tomography models: Application to the greater Alpine region, Geophysical Journal International - GEOPHYS J INT, 176, 542–554, https://doi.org/10.1111/j.1365-246X.2008.03985.x, 2009b.

690    Douglas, A., Bowers, D., and Young, J.: On the onset of P seismograms, Geophysical Journal International, 129, 681–690, 1997.

Dziewonski, A. M., Chou, T.-A., and Woodhouse, J. H.: Determination of earthquake source parameters from waveform data for studies of global and regional seismicity, Journal of Geophysical Research: Solid Earth, 86, 2825–2852, https://doi.org/10.1029/JB086iB04p02825, 1981.

EASI: Eastern Alpine Seismic Investigation, https://doi.org/10.12686/alparray/xt_2014, 2014.

695    Ekström, G., Nettles, M., and Dziewonski, A.: The global CMT project 2004-2010: Centroid-moment tensors for 13,017 earthquakes, Physics of the Earth and Planetary Interiors, 200-201, 1 – 9, https://doi.org/https://doi.org/10.1016/j.pepi.2012.04.002, 2012.

ESI SAS (Earth Science Institute Of The Slovak Academy Of Sciences): National Network of Seismic Stations of Slovakia, https://doi.org/10.14470/FX099882, 2004.

Federal Institute for Geosciences and Natural Resources: German Regional Seismic Network (GRSN), https://doi.org/10.25928/MBX6-HR74, 1976.

Fichtner, A., Kennett, B. L., Igel, H., and Bunge, H.-P.: Full seismic waveform tomography for upper-mantle structure in the Australasian region using adjoint methods, Geophysical Journal International, 179, 1703–1725, 2009.

French Landslide Observatory – Seismological Datacenter / RESIF: Observatoire Multi-disciplinaire des Instabilités de Versants (OMIV), https://doi.org/10.15778/RESIF.MT, 2006.

Gebrande, H., Lüschen, E., Lammerer, B., Oncken, O., Stiller, M., Neubauer, F., Millahn, K., Grassl, H., Bertelli, L., Angeleri, G., Fantoni, R., Mazzotti, A., Bernabini, M., Castellarin, A., and Nicolich, R.: European orogenic processes research transects the eastern Alps, Eos, Transactions American Geophysical Union, 82, 453–461, https://doi.org/https://doi.org/10.1029/01EO00269, 2001.

GEOFON Data Centre: GEOFON Seismic Network, https://doi.org/10.14470/TR560404, 1993.

Geological Survey-Provincia Autonoma Di Trento: Trentino Seismic Network, https://doi.org/10.7914/SN/ST, 1981.

Guéguen, P., Coutant, O., Langlais, M., and RESIF: Maurienne Seismic Swarm 2017-2018, https://doi.org/10.15778/RESIF.YW2017, 2017.

Heit, B., Weber, M., Tilmann, F., Haberland, C., Jia, Y., and Pesaresi, D.: The Swath-D seismic network in Italy and Austria, 2017.

Hetényi, G., Molinari, I., Clinton, J., Bokelmann, G., Bondár, I., Crawford, W. C., Dessa, J.-X., Doubre, C., Friederich, W., Fuchs, F., et al.: The AlpArray seismic network: a large-scale European experiment to image the Alpine orogen, Surveys in geophysics, 39, 1009–1033, 2018.

Hunter, J. D.: Matplotlib: A 2D graphics environment, Computing in Science & Engineering, 9, 90–95, https://doi.org/10.1109/MCSE.2007.55, 2007.

INGV Seismological Data Centre: Rete Sismica Nazionale (RSN), https://doi.org/10.13127/SD/X0FXNH7QFY, 1997.

Institut De Physique Du Globe De Paris (IPGP) and Ecole Et Observatoire Des Sciences De La Terre De Strasbourg (EOST): GEOSCOPE, French Global Network of broad band seismic stations, https://doi.org/10.18715/GEOSCOPE.G, 1982.

Institute Of Geophysics, A. O. S. O. T. C. R.: Czech Regional Seismic Network, https://doi.org/10.7914/SN/CZ, 1973.

Jena, F. S. U.: Thüringer Seismologisches Netz (TSN), https://doi.org/10.7914/SN/TH, 2009.

Kennett, B. L., Engdahl, E., and Buland, R.: Constraints on seismic velocities in the Earth from traveltimes, Geophysical Journal International, 122, 108–124, 1995.

Koulakov, I., Tychkov, S., Bushenkova, N., and Vasilevsky, A.: Structure and dynamics of the upper mantle beneath the Alpine–Himalayan orogenic belt, from teleseismic tomography, Tectonophysics, 358, 77–96, 2002.

Küperkoch, L., Meier, T., Lee, J., Friederich, W., and Group, E.: Automated determination of P-phase arrival times at regional and local distances using higher order statistics, Geophysical Journal International, 181, 1159–1170, https://doi.org/10.1111/j.1365-246X.2010.04570.x, 2010.

Kövesligethy Radó Seismological Observatory (Geodetic And Geophysical Institute, Research Centre For Astronomy And Earth Sciences, Hungarian Academy Of Sciences (MTA CSFK GGI KRSZO)): Hungarian National Seismological Network, https://doi.org/10.14470/UH028726, 1992.

Leipzig University: SXNET Saxon Seismic Network, https://doi.org/10.7914/SN/SX, 2001.

Lippitsch, R., Kissling, E., and Ansorge, J.: Upper mantle structure beneath the Alpine orogen from high-resolution teleseismic tomography, Journal of Geophysical Research, 108, https://doi.org/10.1029/2002JB002016, 2003.

735 Liu, H.-P., Anderson, D. L., and Kanamori, H.: Velocity dispersion due to anelasticity; implications for seismology and mantle composition, Geophysical Journal International, 47, 41–58, 1976.

Malet, J.-P., Hibert, C., Radiguet, M., Gautier, S., Larose, E., Amitrano, D., Jongmans, D., Bièvre, G., and RESIF: French Landslide Observatory – OMIV (Temporary data) (MT-campagne) (RESIF - SISMOB), https://doi.org/10.15778/RESIF.1N2015, 2015.

McKee, K. F., Roman, D., Fee, D., Ripepe, M., AIUPPA, A., and Waite, G.: Seismo-acoustic Network at Stromboli Volcano, Italy,
740 https://doi.org/10.7914/SN/YI_2018, 2018.

MedNet Project Partner Institutions: Mediterranean Very Broadband Seismographic Network (MedNet), https://doi.org/10.13127/SD/FBBBTDTD6Q, 1988.

Mitterbauer, U., Behm, M., Brückl, E., Lippitsch, R., Guterch, A., Keller, G. R., Koslovskaya, E., Rumpfhuber, E.-M., and Šumanovac, F.: Shape and origin of the East-Alpine slab constrained by the ALPASS teleseismic model, Tectonophysics, 510, 195–206, 2011.

745 Monteiller, V., Chevrot, S., Komatitsch, D., and Fuji, N.: A hybrid method to compute short-period synthetic seismograms of teleseismic body waves in a 3-D regional model, Geophysical Journal International, 192, 230–247, https://doi.org/10.1093/gji/ggs006, 2013.

Mora, P.: Nonlinear two-dimensional elastic inversion of multioffset seismic data, Geophysics, 52, 1211–1228, 1987.

OGS (Istituto Nazionale Di Oceanografia E Di Geofisica Sperimentale): North-East Italy Seismic Network, https://doi.org/10.7914/SN/OX, 2016.

750 OGS (Istituto Nazionale Di Oceanografia E Di Geofisica Sperimentale) And University Of Trieste: North-East Italy Broadband Network, https://doi.org/10.7914/SN/NI, 2002.

Piromallo, C. and Morelli, A.: P wave tomography of the mantle under the Alpine-Mediterranean area, Journal of Geophysical Research: Solid Earth, 108, 2003.

Polish Academy of Sciences (PAN) Polskiej Akademii Nauk: Polish Seismological Network, https://www.igf.edu.pl/stacje-en.php, 1990.

755 Rawlinson, N. and Kennett, B. L. N.: Rapid estimation of relative and absolute delay times across a network by adaptive stacking, Geophysical Journal International, 157, 332–340, https://doi.org/10.1111/j.1365-246X.2004.02188.x, 2004.

RESIF: RESIF-RLBP French Broad-band network, RESIF-RAP strong motion network and other seismic stations in metropolitan France, https://doi.org/10.15778/RESIF.FR, 1995.

RESIF: CEA/DASE broad-band permanent network in metropolitan France, https://doi.org/10.15778/RESIF.RD, 2018.

760 Rowe, C. A., Aster, R. C., Borchers, B., and Young, C. J.: An automatic, adaptive algorithm for refining phase picks in large seismic data sets, Bulletin of the Seismological Society of America, 92, 1660–1674, 2002.

Saragiotis, C. D., Hadjileontiadis, L. J., and Panas, S. M.: PAI-S/K: A robust automatic seismic P phase arrival identification scheme, IEEE Transactions on Geoscience and Remote Sensing, 40, 1395–1404, 2002.

Schumacher, F., Friederich, W., and Lamara, S.: A flexible, extendable, modular and computationally efficient approach to scattering-integral-
765 based seismic full waveform inversion, Geophysical Journal International, 204, 1100–1119, https://doi.org/10.1093/gji/ggv505, 2016.

Slovenian Environment Agency: Seismic Network of the Republic of Slovenia, https://doi.org/10.7914/SN/SL, 2001.

Spada, M., Bianchi, I., Kissling, E., Agostinetti, N. P., and Wiemer, S.: Combining controlled-source seismology and receiver function information to derive 3-D Moho topography for Italy, Geophysical Journal International, 194, 1050–1068, 2013.

Swiss Seismological Service (SED) At ETH Zurich: National Seismic Networks of Switzerland,
770 https://doi.org/10.12686/SED/NETWORKS/CH, 1983.

Tesauro, M., Kaban, M. K., and Cloetingh, S. A. P. L.: EuCRUST-07: A new reference model for the European crust, Geophysical Research Letters, 35, https://doi.org/https://doi.org/10.1029/2007GL032244, 2008.

Tong, P., Chen, C.-W., Komatitsch, D., Basini, P., and Liu, Q.: High-resolution seismic array imaging based on a SEM-FK hybrid method, Geophysical Journal International, 197, https://doi.org/10.1093/gji/ggt508, 2014a.

775 Tong, P., Komatitsch, D., Tseng, T.-L., Hung, S.-H., Chen, C.-W., Basini, P., and Liu, Q.: A 3D spectral-element and frequency-wavenumber (SEM-FK) hybrid method for high-resolution seismic array imaging, Geophysical Research Letters, 41, https://doi.org/10.1002/2014GL061644, 2014b.

Tromp, J., Tape, C., and Liu, Q.: Seismic tomography, adjoint methods, time reversal and banana-doughnut kernels, Geophysical Journal International, 160, 195–216, 2005.

780 University Of Genova: Regional Seismic Network of North Western Italy, https://doi.org/10.7914/SN/GU, 1967.

University Of Trieste: Friuli Venezia Giulia Accelerometric Network, https://doi.org/10.7914/SN/RF, 1993.

University Of Zagreb: Croatian Seismograph Network, https://doi.org/10.7914/SN/CR, 2001.

Van Veen, B. D. and Buckley, K. M.: Beamforming: A versatile approach to spatial filtering, IEEE assp magazine, 5, 4–24, 1988.

VanDecar, J. and Crosson, R.: Determination of teleseismic relative phase arrival times using multi-channel cross-correlation and least 785 squares, Bulletin of the Seismological Society of America, 80, 150–169, 1990.

Wielandt, E.: On the validity of the ray approximation for interpreting delay times, in: Seismic tomography, pp. 85–98, Springer, 1987.

ZAMG - Central Institute for Meteorology and Geodynamics: Province Südtirol, 2006.

ZAMG-Zentralanstalt Für Meterologie Und Geodynamik: Austrian Seismic Network, https://doi.org/10.7914/SN/OE, 1987.

Zhao, L., Paul, A., Malusà, M., Xiaobing, X., Zheng, T., Solarino, S., Guillot, S., Schwartz, S., Dumont, T., Salimbeni, S., Aubert, C., Pon-790 drelli, s., Wang, Q., and Zhu, R.: Continuity of the Alpine slab unraveled by high-resolution P-wave tomography, Journal of Geophysical Research: Solid Earth, 121, https://doi.org/10.1002/2016JB013310, 2016.

Zhu, H., Bozdağ, E., Peter, D., and Tromp, J.: Structure of the European upper mantle revealed by adjoint tomography, Nature Geoscience, 5, 493–498, 2012.

Zhu, H., Bozdağ, E., and Tromp, J.: Seismic structure of the European upper mantle based on adjoint tomography, Geophysical Journal 795 International, 201, 18–52, 2015.